Monthly Notices
of the
ROYAL ASTRONOMICAL SOCIETY

Mon. Not. R. Astron. Soc. **411,** 2667–2694 (2011) doi:10.1111/j.1365-2966.2010.17874.x

The massive galaxy cluster XMMU J1230.3+1339 at $z \sim 1$: colour–magnitude relation, Butcher–Oemler effect, X-ray and weak lensing mass estimates⋆

M. Lerchster,[1,2,3]† S. Seitz,[1,2] F. Brimioulle,[1] R. Fassbender,[2] M. Rovilos,[2] H. Böhringer,[2] D. Pierini,[2] M. Kilbinger,[1,3] A. Finoguenov,[2,4] H. Quintana[5] and R. Bender[1,2]

[1]*University Observatory Munich, Ludwigs-Maximilians University Munich, Scheinerstr. 1, 81679 Munich, Germany*
[2]*Max-Planck-Institute for extraterrestrial Physics, Giessenbachstraße, 85748 Garching, Germany*
[3]*Excellence Cluster Universe, Technical University Munich, Boltzmannstr. 2, 85748 Garching, Germany*
[4]*University of Maryland, Baltimore County, 1000 Hilltop Circle, Baltimore, MD 21250, USA*
[5]*Pontificia Universidad Catolica de Chile, Department of Astronomy and Astrophysics, Casilla 306, Santiago, Chile*

Accepted 2010 October 14. Received 2010 October 7; in original form 2010 August 6

ABSTRACT

We present results from the multiwavelength study of XMMU J1230.3+1339 at $z \sim 1$. We analyse deep multiband wide-field images from the Large Binocular Telescope (LBT), multi-object spectroscopy observations from VLT, as well as space-based serendipitous observations, from the *GALEX* and *Chandra* X-ray observatories. We apply a Bayesian photometric redshift code to derive the redshifts using the far-UV (FUV), near-UV (NUV) and the deep U, B, V, r, i, z data. We make further use of spectroscopic data from FORS2 to calibrate our photometric redshifts, and investigate the photometric and spectral properties of the early-type galaxies. We achieve an accuracy of $\triangle z/(1+z) = 0.07$ (0.04) and the fraction of catastrophic outliers is $\eta = 13$ (0) per cent, when using all (secure) spectroscopic data, respectively. The $i - z$ against z colour–magnitude relation of the photo-z members shows a tight red sequence with a zero-point of 0.935 mag, and slope equal to -0.027. We observe evidence for a truncation at the faint end of the red-cluster-sequence and the Butcher–Oemler effect, finding a fraction of blue galaxies $f_b \approx 0.5$. Further, we conduct a weak lensing analysis of the deep 26×26 arcmin r-band LBC image. The observed shear is fitted with a Single-Isothermal-Sphere and a Navarro–Frenk–White model to obtain the velocity dispersion and the model parameters, respectively. Our best-fitting values are, for the velocity dispersion $\sigma_{\rm SIS} = 1308 \pm 284\,{\rm km\,s^{-1}}$, concentration parameter $c = 4.0^{+14}_{-2}$ and scale radius $r_{\rm s} = 345^{+50}_{-57}$ kpc. From a 38 ks *Chandra* X-ray observation we obtain an independent estimate of the cluster mass. In addition, we create a signal-to-noise ratio (S/N) map for the detection of the matter mass distribution of the cluster using the mass-aperture technique. We find excellent agreement of the mass concentration identified with weak lensing and the X-ray surface brightness. Combining our mass estimates from the kinematic, X-ray and weak lensing analyses we obtain a total cluster mass of $M^{\rm tot}_{200} = (4.56 \pm 2.3) \times 10^{14}\,{\rm M}_{\odot}$. This study demonstrates the feasibility of ground-based weak lensing measurements of galaxy clusters up to $z \sim 1$.

Key words: gravitational lensing – galaxies: clusters: individual: XMMU J1230.3+1339 – galaxies: fundamental parameters – X-rays: galaxies: clusters.

⋆Based on data acquired using the Large Binocular Telescope (LBT). The LBT is an international collaboration among institutions in the United States, Italy and Germany. LBT Corporation partners are the University of Arizona on behalf of the Arizona university system; Istituto Nazionale di Astrofisica, Italy; LBT Beteiligungsgesellschaft, Germany, representing the Max-Planck Society, the Astrophysical Institute Potsdam, and Heidelberg University; Ohio State University, and the Research Corporation, on behalf of the University of Notre Dame, the University of Minnesota and the University of Virginia. Also based on observations made with ESO Telescopes at the La Silla or Paranal Observatories program ID 081.A-0312. This research has made use of data obtained from the *Chandra* Data Archive and software provided by the *Chandra* X-ray Centre (CXC) in the application packages CIAO, CHIPS and SHERPA.

†E-mail: mike@usm.lmu.de; mlerchst@mpe.mpg.de

1 INTRODUCTION

Clusters of galaxies are receiving an increasing interest in astronomical studies since the last decade for a variety of reasons. They are the largest gravitationally bound objects in the universe and provide ideal organized laboratories for the cosmic evolution of baryons, in the hot Intra-Cluster Medium (ICM) phase and galaxies. They are also ideal tracers of the formation of the large-scale structure.

The combination of optical, spectroscopic, lensing and X-ray studies allows us to get important insights into physical properties of the cluster members, the ICM and the determination of the gravitational mass and its distribution with independent methods. The dynamical state of the ICM can also reveal information about the recent merger history, thus providing an interesting way to test the concept of hierarchical cluster formation, as predicted in the cold dark matter (CDM) paradigm.

In the past, clusters of galaxies have been the subject of combined weak lensing and dynamical studies (e.g. Radovich et al. 2008), weak and strong lensing plus X-ray studies (e.g. Kausch et al. 2007), and weak lensing and X-ray studies (e.g. Hoekstra 2007). In addition, Taylor et al. (2004) for ground-based data and Heymans et al. (2008) for space-based data showed for the $z = 0.16$ supercluster A901/2 (COMBO-17 survey) that a three-dimensional (3D) lensing analysis combined with photometric redshifts can reveal the 3D dark matter distribution to high precision.

Wide-field instruments, such as the European Southern Observatory (ESO) Wide-Field Imager (WFI) at the ESO 2.2 m with a field of view (FOV) of 34×33 arcmin^2, the MEGAPRIME instrument mounted at the 3.6 m Canada–France–Hawaii Telescope (CFHT) with an FOV of $\approx$1 deg^2, the Suprime-Cam with an FOV of 34×27 arcmin^2 at the 8.2-m Subaru telescope and, more recently, the Large Binocular Camera (LBC) instruments mounted at the 8.4 m Large Binocular Telescope (LBT; Hill & Salinari 1998) with an FOV of 26×26 arcmin^2, are particularly well suited for the multiband and weak lensing studies of clusters. One can obtain multiband photometry for evolution studies based on spectral energy distribution (SED) fitting techniques and one can also apply weak lensing studies to the clusters, because the FOV is capable of sampling the signal well beyond the cluster size.

In this paper, we present a combined optical, kinematic, weak lensing and X-ray analysis of XMMU J1230.3+1339. This cluster of galaxies is located at $\alpha = 12^{\rm h}30^{\rm m}18^{\rm s}, \delta = +13^\circ39'00''$ (J2000), redshift $z_{\rm cl} = 0.975$ and Abell richness[1] class 2 (see Fassbender et al. 2010, hereafter Paper I, for more details). The cluster was detected within the framework of the XMM–Newton Distant Cluster Project (XDCP) described in Fassbender (2008).

We combine optical six-band data, multi-object spectroscopy data, space-based UV data (*GALEX*) and X-ray (*Chandra*) data. In this work we present a detailed analysis of the optical data, estimating photometric redshifts and performing an SED classification, exploring the colour–magnitude and colour–colour relations. Based on this, we conduct a weak lensing analysis and estimate, independently and self-consistently, the cluster mass from X-ray, kinematics and weak lensing, complementing the analysis presented in Paper I. In Section 2, we give an overview of the data acquisition and reduction. We briefly outline the reduction of the LBC data and describe the acquisition of the spectroscopic redshifts in Section 2. In Section 3 we explain the method used to derive the photometric catalogues and redshifts; we discuss the accuracy of the derived redshifts for the cluster and show the distribution of its galaxies. In Section 4, we present the weak lensing analysis (mass distribution) and constraints for the clusters, whereas the estimates for the kinematic analysis (velocity dispersion) are shown in Section 5. The X-ray analysis (surface-brightness profile, global temperature) is presented in Section 6, and the mass estimates are shown in Section 7. We discuss and summarize our findings in Sections 8 and 9.

Throughout the paper, we assume a ΛCDM cosmology with $\Omega_{\rm M} = 0.27$, $\Omega_\Lambda = 0.73$ and $H_0 = 72\,{\rm km\,s^{-1}\,Mpc^{-1}}$. Therefore, 1 arcsec angular distance corresponds to a physical scale of 7.878 kpc at the cluster redshift.

2 DATA ACQUISITION AND REDUCTION

2.1 Optical ground-based data

In Table 1, we summarize the properties (e.g. instrument, filter, exposure time, seeing) of all optical data used in this analysis. The limiting magnitude quoted in Column 8 is defined as the 5σ detection limit in a 1.0 arcsec aperture via:

$$m_{\rm lim} = {\rm ZP} - 2.5 * \log(5\sqrt{N_{\rm pix}}\sigma_{\rm sky}), \quad (1)$$

where ZP is the magnitude zero-point, $N_{\rm pix}$ the number of pixels in a circle with radius 1.0 arcsec and $\sigma_{\rm sky}$ the sky background noise variation. Since this equation assumes Poissonian noise whereas the noise of reduced, stacked data is typically correlated, this estimate represents an upper limit.

2.1.1 LBC-observations and data reduction

We observed XMMU J1230.3+1339 in six optical broad bands (U, B, V, r, i, z), with the 8.4 m LBT and the LBC instruments in 'binocular' mode in an observing run from 2009.02.28 until 2009.03.02 The LBC cameras (see e.g. Giallongo et al. 2008; Speziali et al. 2008) have a 4 CCD array (2048×4096 pixel in each CCD; 0.224 arcsec pixel scale; 26×26 arcmin^2 total field-of-view). Three chips are aligned parallel to each other while the fourth is rotated by 90° and located above them. The U, B, V images were obtained with the blue sensitive instrument (3500–9000 Å) and in parallel to the r, i, z images with the red sensitive instrument (5000–10 000 Å). In Figs. 1, 2 and 3 we show the LBT i-band image FOV 6×6 arcmin^2, FOV 3×3 arcmin^2 and a three-color image, respectively. For the single frame reduction and the creation of image stacks for the scientific exploitation, we follow the method described in detail in Rovilos et al. (2009). Here, we quickly summarize the most important reduction steps.

(1) Single frame standard reduction (e.g. bias correction, flat-fielding, defringing).

(2) Quality control of all four chips of each exposure to identify bad ones (e.g. chips with a large fraction of saturated pixels, etc.).

(3) Identification of satellite tracks by visual inspection and creation of masks.

(4) Creation of weight images with WEIGHTWATCHER (Bertin & Marmo 2007) for each chip, accounting for bad pixels and the satellite track masks.

(5) Extraction of catalogues with SEXTRACTOR (Bertin & Arnouts 1996) for astrometric calibration.

(6) Astrometric calibration with the USNO-A2 astrometric catalogue (Monet 1998) using the IRAF CCMAP package. This yields an external accuracy with an *rms* of 0.25 arcsec and an internal accuracy with an *rms* of 0.066 arcsec (Rovilos et al. 2009).

[1] See richness definition in Abell et al. (1989).

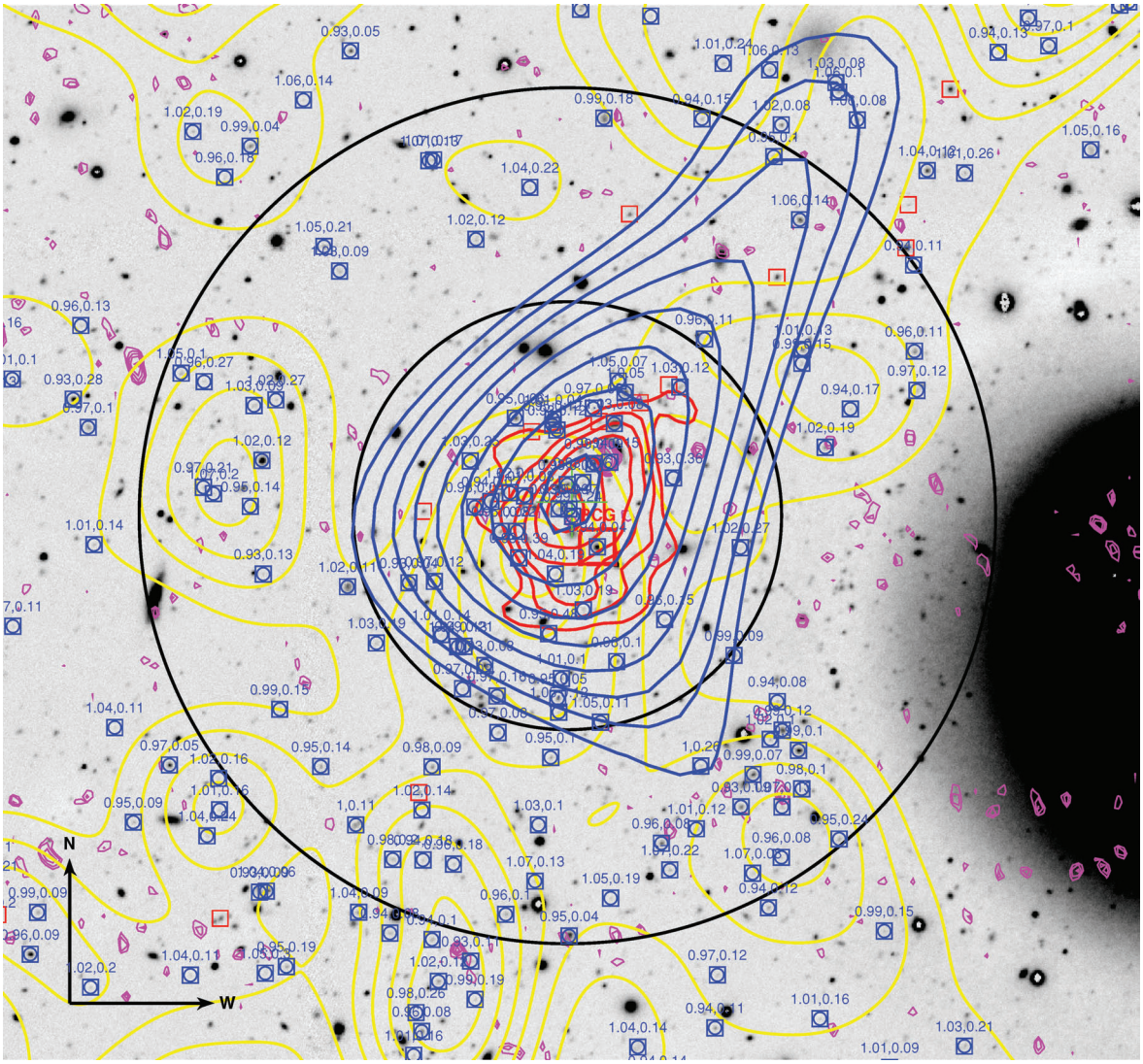

Figure 1. XMMU J1230.3+1339 at $z = 0.975$: 6 × 6 arcmin LBT-i-band image (5.94 ks), overlaid with colour-coded contours. In yellow: the surface brightness contours of the smoothed light of cluster members, selected to lie at $z_{\rm cluster} - 0.05 \leq z_{\rm phot} \leq z_{\rm cluster} + 0.05$; in blue: weak lensing $M_{\rm ap}$ significance contours (1–5); in red: X-ray contours (0.3–2.4 keV); in magenta: VLA-FIRST (0.3–0.9 mJy) contours. The red big box marks the location of the BCG, the red small boxes mark the high confidence spectroscopic confirmed members (13), the blue small boxes (numbers are redshift and error) mark the photo-z selected cluster members and the black circles mark a radius of 0.5 and 1 Mpc from the cluster centre, respectively (note: $r_{200} \approx 1$ Mpc). The large object to the west is the foreground galaxy NGC 4477.

Table 1. Cluster optical data overview.

Field/area (deg^2)	Telescope/instrument	FOV (arcmin*arcmin)	Filter	N^a	Expos. time (s)	Zero-point (AB mag)	$m_{\rm lim}$ ^{b} (AB mag)	Seeing (arcsec)	$\sigma_{\rm sky}$ (ADU)
XMMU J1230.3+1339	LBT/LBCB	26*26	*U*	24	4320	32.22	26.97	0.85	3.2
(0.19)	LBT/ LBCB	26*26	*B*	17	3060	32.98	26.90	0.87	6.9
	LBT/LBCB	26*26	*V*	13	2340	33.27	26.32	0.85	15.3
	LBT/LBCR	26*26	r^c	12	2160	33.44	26.18	0.95	20.3
	LBT/LBCR	26*26	*i*	27	4860	33.27	25.80	0.87	24.5
	LBT/LBCR	26*26	*z*	44	7960	32.79	25.37	0.78	23.5

[a]Number of single exposures ($t_{\rm exp} = 180$ s) used for the final stack.
[b]The limiting magnitude is defined in equation (1).
[c]Lensing band.

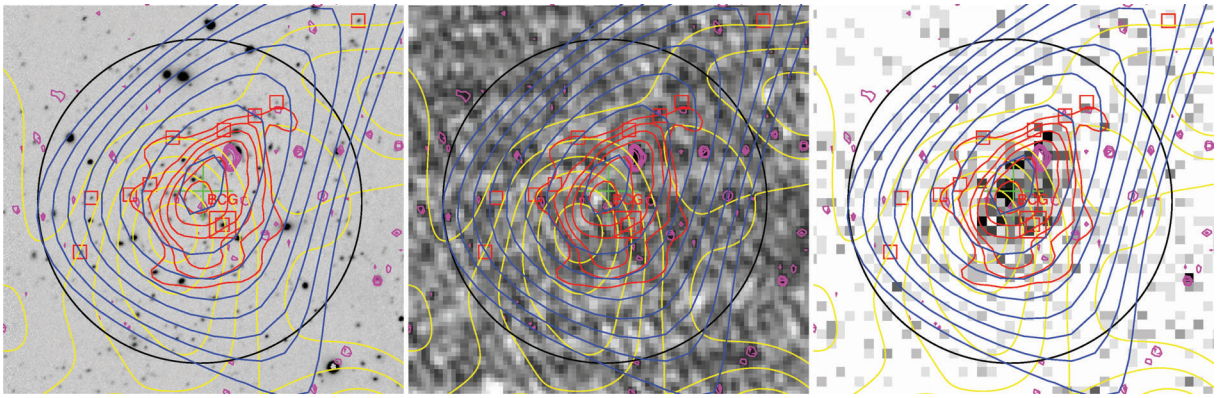

Figure 2. Left-hand panel: same as Fig. 1 for the inner 0.5 Mpc (black circle) of the cluster, FOV 3 × 3 arcmin^2. Middle panel: VLA-FIRST 1.4 GHz-band image overlaid with colour-coded contours. Right-hand panel: X-ray (0.6–2.4 keV) image overlaid with colour-coded contours. In yellow the luminosity contours of the cluster members, selected to lie at $z_{\rm cluster} - 0.05 \leq z_{\rm phot} \leq z_{\rm cluster} + 0.05$, in blue weak lensing $M_{\rm ap}$ significance contours (1–5) and in red X-ray contours (0.6–2.4 keV).

(7) Flux calibration with standard star observations in each of our six bands using Landolt standards or Sloan Digital Sky Survey (SDSS) DR7.

(8) Background subtraction and measure of the variation of $\sigma_{\rm sky}$ of each exposure to identify bad images (e.g. those with a value 3σ above the median value).

(9) Point spread function (PSF) control of all exposures to identify bad patterns (e.g. strong variation of the direction and amplitude of the measured star ellipticity on each chip of each exposure, etc.).

(10) Co-addition with the SWARP software (Bertin 2008). Note that we do not consider exposures with full width at half-maximum (FWHM) > 1.0 arcsec.

(11) Masking of the image stacks to leave out low-SNR regions and regions affected by stellar diffraction spikes and stellar light haloes as well as asteroid tracks.

The number of frames which remain in this procedure is different from band to band (see Column 5 in Table 1). Starting from 50, 33, 20, 20, 33, 50 images in the U, B, V, r, i, z filters, we at the end only stack 24, 17, 13, 12, 27, 44 frames for the photometric and weak lensing analyses. In Fig. 4 we show as an example one 'good' and one 'bad' single frame exposure.

We derive our number counts by running SEXTRACTOR on the final image stacks with the corresponding weight map. We convolve the data with a Gaussian kernel and require for a detection to have four contiguous pixels exceeding a signal-to-noise ratio (S/N) of 1.25 on the convolved frame. Stars are then identified in the stellar locus, plotting the magnitude versus the half-light radius in Fig. 20 and identify high S/N but unsaturated stars. In Fig. 5, we show the achieved number counts for the final image stacks. Table 1 summarizes the properties of each image stack. For comparison we plot in Fig. 5, for the *U, B, V* bands, the number counts derived from Rovilos et al. (2009) for the deep Lockman Hole observation with the LBT. We do not show the uncertainties for these literature results, which have large errors at the bright end (U, B, V mag <22.5). In addition, we compare our *B, V, r* and *i* band number counts to those from McCracken et al. (2003) for the VVDS Field. For the z band the comparison is with the number counts from Erben et al. (2009) for the CFHTLS D1 Field. In terms of amplitude and slope, our agreement with the literature measurements is very good. The comparison of our data to deeper literature data and the linear number count fits added with a solid line shows that the 50 per cent completeness for an extended galaxy roughly falls together with the prediction for a point source within a 2 arcsec diameter aperture (long dashed line) according to equation (1).

2.2 Spectroscopy

In Table 2, we give an overview of all spectroscopic data used in this analysis.

2.2.1 VLT spectroscopy and data reduction

For the kinematic study of the cluster and the calibration of the photometric redshifts we use the data taken in 2008 April and 2008 June with the FOcal Reducer and low dispersion Spectrograph (FORS) mounted at the UT1 of the Very Large Telescope (VLT), which were taken as part of the VLT-program 081.A-0312 (PI: H. Quintana). The MOS/MXU spectroscopy was performed with FORS2 (see e.g. Appenzeller et al. 1998) in medium-resolution ($R = 660$) mode (grism GRIS_300I+21). The data were reduced using the IRAF[2] software package. For the redshift determination (redshift, error, confidence level) the spectra were cross-correlated with template spectra using the IRAF package RVSAO. More details can be found in Paper I.

The spectroscopic observations provide 38 spectra, where 17 of them matched in position with objects from our photometric catalogue. For the comparison to photometric redshifts we consider galaxies with trustworthy $\geq$95 per cent confidence spectroscopic redshifts only. Due to low S/N (at high redshift) and the limited wavelength ranges of the spectra only eight objects could be considered.

We have been awarded additional FORS2 spectroscopy for $\sim$100 photo-z selected cluster members; the analysis of these data will be described in an upcoming paper.

[2] http://iraf.noao.edu

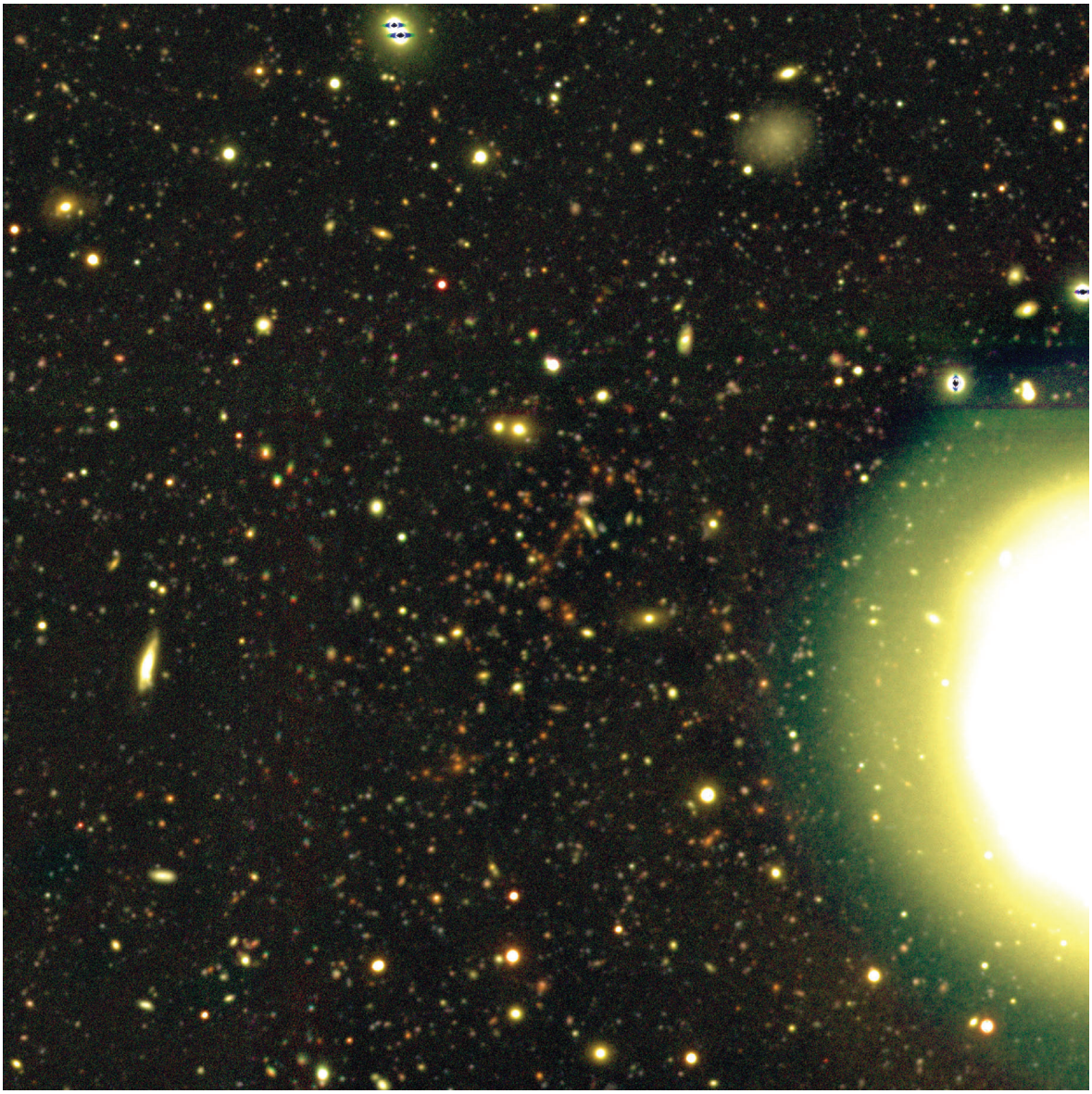

Figure 3. The 6 × 6 arcmin^2, three-colour image of the cluster XMMU J1230.3+1339, with r-channel (5.94 ks *i* band), g-channel (3.24 ks *r* band) and b-channel (5.94 ks *B* band) colours. The cluster members appear as reddish objects. The large, yellowish object on the right-hand side is the foreground galaxy NGC 4477 .

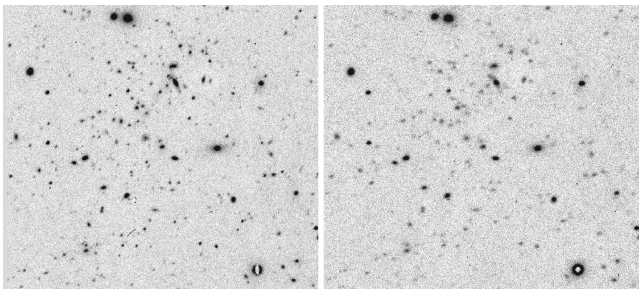

Figure 4. LBT *i*-band single frames: the left-hand panel shows a 'good' frame (FWHM 0.64 arcsec) whereas the right-hand panel shows a 'bad' one (FWHM 1.20 arcsec).

2.2.2 *SDSS spectroscopy*

The field of XMMU J1230.3+1339 has complete overlap with the SDSS[3]. Via the flexible web-interface SkyServer[4] of the Catalog Archive Server (CAS), we get access to the redshift catalogue. For our purpose, we only consider objects clearly classified as a galaxy with a redshift ≥ 95 per cent confidence. By matching the SDSS catalogue with our catalogue we find 13 objects with spectroscopic redshifts between 0 and 0.6 in the SDSS-DR7

[3] Funding for the SDSS and SDSS-II has been provided by the Alfred P. Sloan Foundation, the Participating Institutions, the National Science Foundation, the US Department of Energy, the National Aeronautics and Space Administration, the Japanese Monbukagakusho, the Max Planck Society and the Higher Education Funding Council for England. The SDSS Web Site is http://www.sdss.org/.

[4] http://cas.sdss.org/astro/en/tools/search/SQS.asp

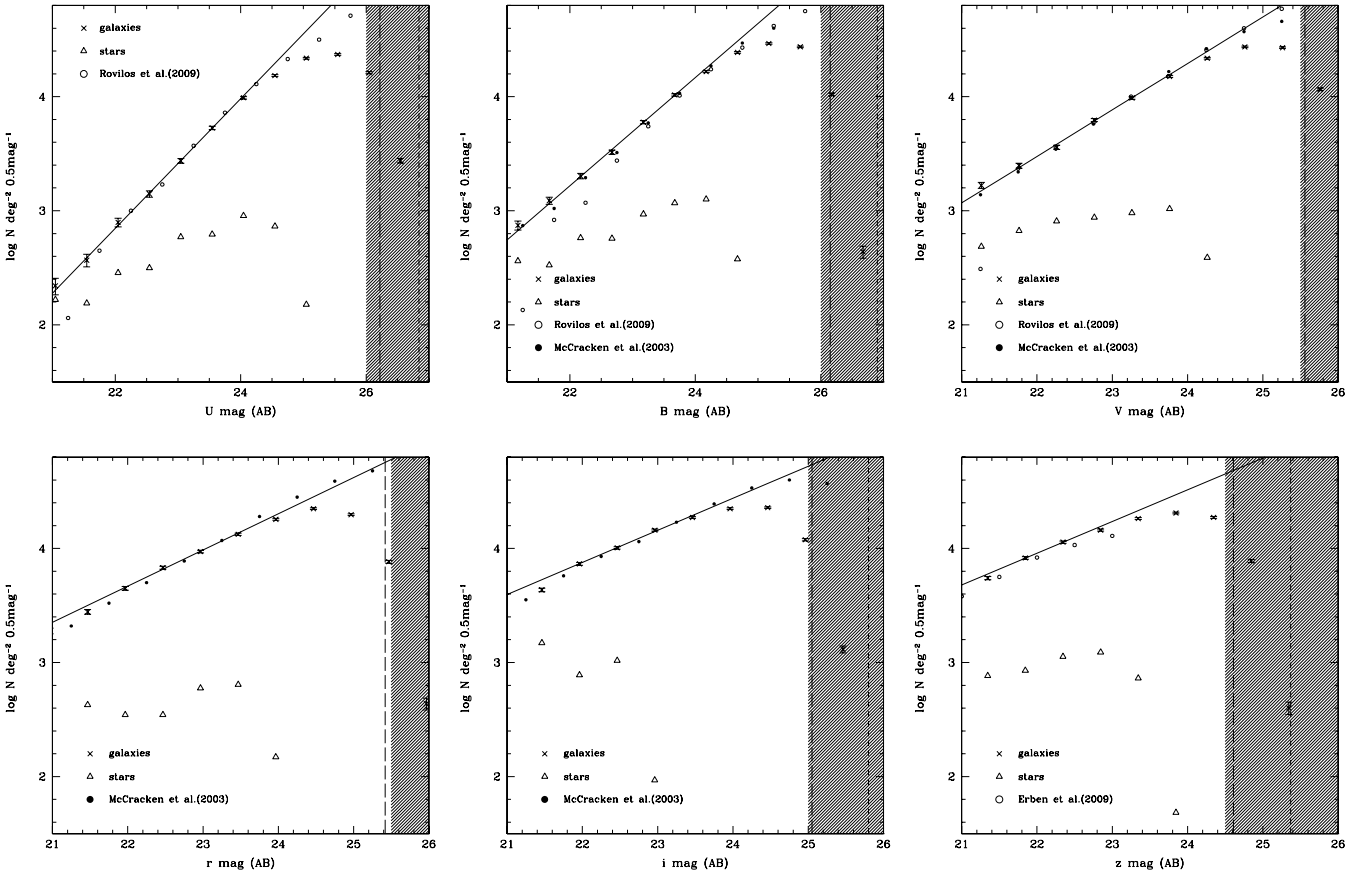

Figure 5. Number counts per 0.5 mag and square degree of galaxies (crosses) and stars (open triangles) for the image stacks in the six (U, B, V, r, i, z) filters. The black line shows a linear fit to the galaxies number counts. For comparison we plot the number counts (open circles) derived from Rovilos et al. (2009) and (filled circles) McCracken et al. (2003), see text for details. The short/long dashed lines indicate the estimated limiting magnitudes, respectively, defined as a point source 5σ detection limit in a 1.0/2.0 arcsec aperture. We used equation (1) for the noise levels of the image stacks listed in Table 1. By comparing our number counts to deeper literature data and the extrapolation of the linear fit we can estimate the 50 per cent completeness for the detection. We have shaded the region where the completeness drops below 50 per cent in each filter.

(Adelman-McCarthy et al. 2007). For the comparison to photometric redshifts we consider 10 of the 13 objects for which the confidence level is larger than 3.

2.3 *GALEX* UV data

We include near-UV (NUV; 1770–2730 Å) and far-UV (FUV; 1350–1780 Å) data from the Galaxy Evolution Explorer[5] (*GALEX*). The instrument provides simultaneous co-aligned FUV and NUV images with spatial resolution of 4.3 and 5.3 arcsec, respectively, with FOV of $\approx 1\overset{\circ}{.}2$. The zero-points have been taken from *GALEX* Observers's Guide,[6] $\mathrm{ZP_{FUV}} = 18.82\,\mathrm{mag}_{AB}$ and $\mathrm{ZP_{NUV}} = 20.08\,\mathrm{mag}_{AB}$.

We use data taken during the nearby galaxy survey (NGS) and the guest investigator program (GII) and publicly released in the GR4. In total, we make use of three pointings, GI1_109010_NGC4459, NGA_Virgo_MOS09 and NGA_Virgo_MOS11, with a total exposure time of ≈8.4 ks in NUV and ≈3.0 FUV. After retrieving the data from the web-interface MAST,[7] we further process them with publicly available tools[8] (SCAMP, SWarp) and obtain resampled and stacked images.

The *GALEX* data are rather shallow. Nevertheless, they are useful to improve the quality of the photometric redshifts, in particular to disentangle SED degeneracies in the blue part of the spectra as detailed in Gabasch et al. (2008). Fig. 6 shows that some galaxies can clearly be detected in the *GALEX* filters (FUV, NUV), e.g. foreground spiral galaxy above the brightest cluster galaxy (BCG) shows an NUV excess.

2.4 X-ray data

2.4.1 Chandra observations

We use the archival observation by *Chandra* (PI: Sarazin, Obs-Id 9527), as listed in Table 3. The cluster centre lies on the S3 chip of the Advanced CCD Imaging Spectrometer (ACIS) array. The observation was conducted in VFAINT mode, and reprocessed accordingly using the *Chandra* software[9] CIAO 4.1 (Friday, 2008 December 5) and related calibration files, starting from the level 1 event file. We used the CIAO 4.1 tools ACIS_PROCESS_EVENTS, ACIS_RUN_HOTPIX

[5] http://galex.caltech.edu
[6] http://galexgi.gsfc.nasa.gov/docs/galex/Documents/ERO_data_description_2.htm
[7] http://galex.stsci.edu/GR4/
[8] http://astromatic.iap.fr/
[9] http://cxc.harvard.edu/ciao

Table 2. Spectroscopic data overview.

ID	RA (○)	Dec. (○)	MAG_AUTO i_{AB}	z_{spec} [a]	Flag[b]	Ref.[c]	Comments
34	187.5598939	13.7739387	17.1514	0.1300	4	1	
35	187.6228679	13.7854572	16.8121	0.1573	4	1	
44	187.5528796	13.4550020	16.5786	0.0830	4	1	
46	187.5733437	13.4931093	16.3311	0.0832	4	1	
47	187.5878466	13.4371208	17.0668	0.0838	4	1	
50	187.6041016	13.4623009	16.2996	0.0829	4	1	
57	187.3367446	13.6621547	20.2306	0.3918	4	1	
58	187.4747995	13.6681400	17.4096	0.1447	4	1	
59	187.4367670	13.5817725	18.3299	0.4377	4	1	
61	187.6479182	13.6215654	18.3519	0.2439	4	1	
67	187.5400466	13.6773148	24.3561	0.9642	4	2	[O II] emitter
69	187.5498491	13.6759957	22.0181	0.9691	4	2	
80	187.5740730	13.6573756	21.9994	0.9758	4	2	
82	187.5681276	13.6472714	20.8572	0.9786	3	2	BCG
83	187.5767988	13.6519471	22.2796	0.9793	3	2	
84	187.5791935	13.6507665	22.2532	0.8616	3	2	
85	187.5838292	13.6503877	22.8933	0.9690	4	2	
86	187.5851446	13.6441070	21.9350	0.9767	4	2	

[a]Measurement error: $\sigma_z \sim 0.0002$.
[b]Flags and confidence classes – 0: no redshift, 1: 50 per cent confidence, 2: 75 per cent confidence, 3: 95 per cent confidence, 4: 100 per cent confidence.
[c]1: Adelman-McCarthy et al. (2007); 2: Paper I.

to flag and remove bad X-ray events, which are mostly due to cosmic rays. A charge transfer inefficiency (CTI) correction is applied during the creation of the new level 2 event file.[10] This kind of procedure reduces the ACIS particle background significantly compared to the standard grade selection,[11] whereas source X-ray photons are practically unaffected (only about 2 per cent of them are rejected, independent of the energy band, provided there is no pileup[12]). Upon obtaining the data, aspect solutions were examined for irregularities and none was detected. Charged particle background contamination was reduced by excising time intervals during which the background count rate exceeded the average background rate by more than 20 per cent, using the CIAO 4.1 LC_CLEAN routine, which is also used on the ACIS background files.[13] Bad pixels were removed from the resulting event files, and they were also filtered to include only standard grades 0, 2, 3, 4 and 6. After cleaning, the available exposure time was 36145 s.

Images, instrument maps and exposure maps were created in the 0.5–7.0 keV band using the CIAO 4.1 tools DMCOPY, MKINSTMAP and MKEXPMAP, binning the data by a factor of 2. Data with energies above 7.0 keV and below 0.5 keV were excluded due to background contamination and uncertainties in the ACIS calibration, respectively. Flux images were created by dividing the image by the exposure map, and initial point source detection was performed by running the CIAO 4.1 tools WTRANSFORM and WRECON on the 0.4–5.0 keV image. These tools identify point sources using 'Mexican Hat' wavelet functions of varying scales. An adaptively smoothed flux image was created with CSMOOTH. This smoothed image was used to determine the X-ray centroid of the cluster, which lies at an RA, Dec. of 12:30:17.02, +13:39:00.94 (J2000). The uncertainty associated with this position can be approximated by the smoothing scale applied to this central emission (2.5 arcsec). Determined in this manner, the position of the X-ray centroid is 15 ± 2.5 arcsec ($110.85 \pm 18.5\, h_{72}^{-1}$ kpc) from the BCG of XMMU J1230.3+1339. Fig. 2 shows an LBT image of XMMU J1230.3+1339 with adaptively smoothed X-ray flux contours overlaid.

2.5 Radio data

For the identification of X-ray point sources we make use of Faint Images of the Radio Sky at 20-cm from the FIRST survey (see Becker, White & Helfand 1995). Using the NRAO Very Large Array (VLA) and an automated mapping pipeline, images with 1.8 arcsec pixels, a typical rms of 0.15 mJy and a resolution of 5 arcsec are produced, and we retrieve these data through the web-interface.[14]

Figs 1 and 2 show LBT images of XMMU J1230.3+1339 with smoothed radio contours overlaid (see Paper I for more details).

3 OPTICAL ANALYSIS

In this section, we give an overview of the catalogue creation, the photometric redshift estimation and the galaxy classification. Furthermore, we describe in detail the construction of luminosity maps and the colour–magnitude relation (CMR).

3.1 Photometric catalogues

For the creation of the multicolour catalogues we first cut all images in the filter U, B, V, r, i, z to the same size. After this, we measure the seeing in each band to find the band with the worst seeing. We then degrade the other bands with a Gaussian filter to the seeing according to the worst band. For the object detection we

[10] http://cxc.harvard.edu/ciao/threads/createL2/
[11] http://asc.harvard.edu/cal/Links/Acis/acis/Cal_prods/vfbkgrnd
[12] http://cxc.harvard.edu/ciao/ahelp/acis_pileup.html
[13] http://cxc.harvard.edu/ciao/threads/acisbackground/
[14] http://third.ucllnl.org/cgi-bin/firstcutout

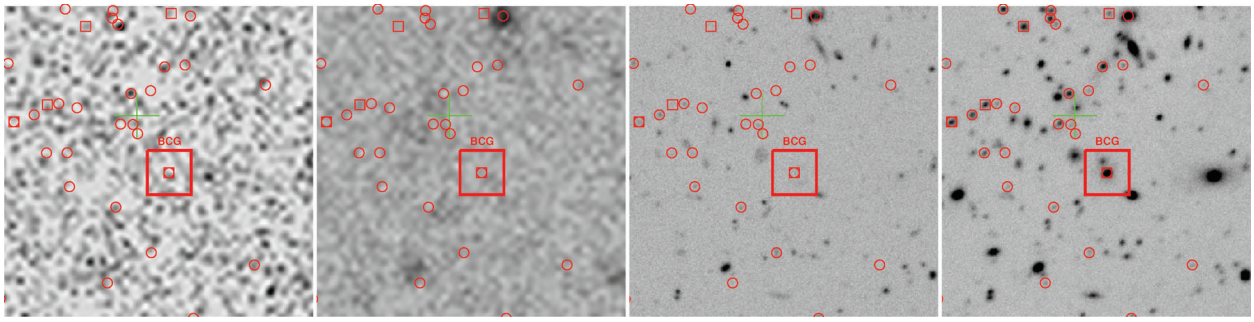

Figure 6. 1.5× 1.5 arcmin^2 zoom at the BCG (large red box) in *FUV*-, *NUV-GALEX, LBT-U* and *LBT-i* band, overlaid (red circle) galaxies used in our photometric analysis. Small red boxes mark objects with spectroscopic redshifts.

Table 3. Cluster X-ray data overview.

Object	Telescope	Instrument	Filter/mode	Total exposure	Clean exposure (s)	Net counts[a]	Obs ID	Comments
XMMU J1230.3+1339	*Chandra*	ACIS-S	VFAINT	37681	36145	639	9527	chip S3

[a]Number of net detected counts in the 0.5–2 keV band.

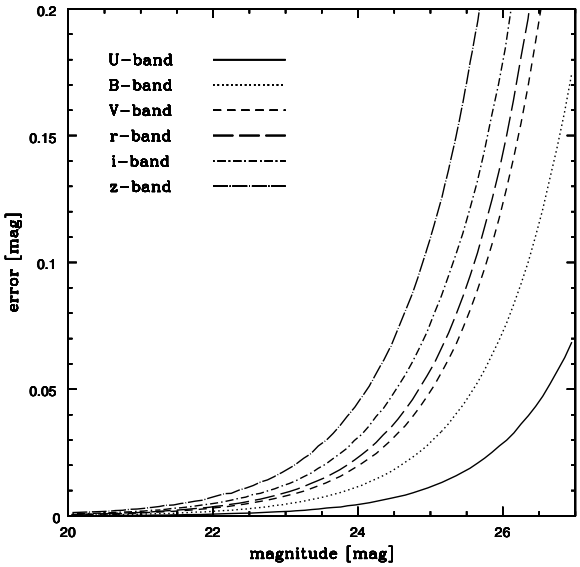

Figure 7. Photometric error as a function of apparent magnitude in the six (U, B, V, r, i, z) filters.

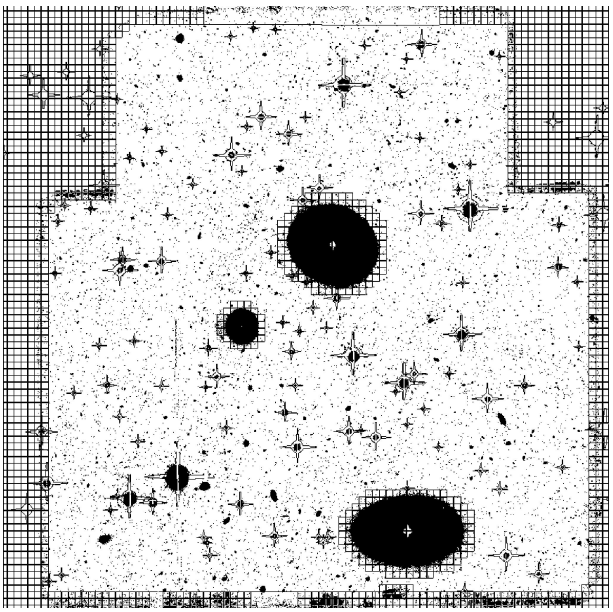

Figure 8. Semi-automatic image masking for the 26 × 26 arcmin^2 LBT field. The polygon squares mark objects from the density analysis and the stars cover sources identified in the GSC-1, GSC-2 and USNO-A2 Standard Star Catalogues [see Erben et al. (2009) for further details].

use SExtractor in dual-image mode, using the unconvolved *i*-band image as the detection image, and measure the fluxes for the colour estimations and the photometric redshifts on the convolved images. We use a Kron-like aperture (MAG_AUTO) for the total magnitudes of the objects, and a fixed aperture (MAG_APER) of ≈ 2 arcsec diameter (corresponding to ≈15 kpc at the cluster redshift) for the colours of the objects. Fig. 7 shows the median photometric error as a function of apparent magnitude for the different filters. The magnitude error is from SExtractor which does not consider correlated noise. Comparing the formal magnitude error with the 50 per cent detection limits suggests a scaling of a factor of 2. To account for Galactic extinction we apply the correction factor $E(B-V) = 0.022$ retrieved from the NASA Extragalactic Data base,[15] from the dust extinction maps of Schlegel, Finkbeiner & Davis (1998), to our photometric catalogue.

To account for extended haloes of very bright stars, diffraction spikes of stars, areas around large and extended galaxies and various kinds of image reflections we generate a mask, shown in Fig. 8. We do not consider objects within these masks in the photometric and shape catalogue later on.

3.2 Photometric redshifts

We use the Bayesian PHOTO-z code (Bender et al. 2001) to estimate the photometric redshifts. The method is similar to that described by Benítez (2000). The redshift probability for each SED type is obtained from the likelihood according to the χ^2 of the photometry

[15] http://nedwww.ipac.caltech.edu/

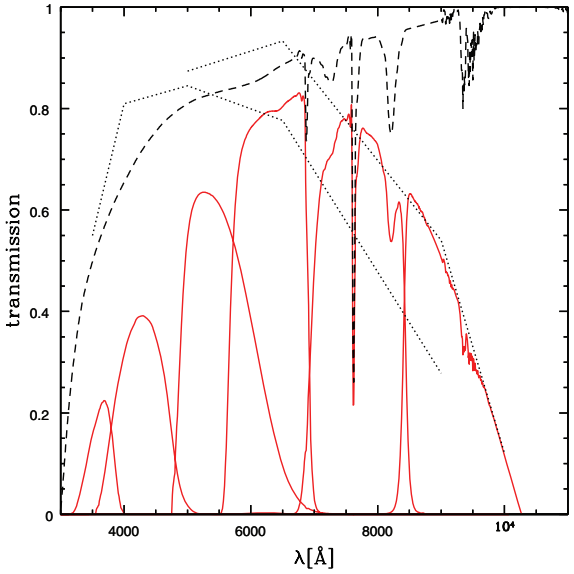

Figure 9. Transmission curves of the six (Bessel-like *U*, *B*, *V* from LBCB; Sloan-like *r*, *i*, *z* from LBCR) filters. The dotted lines show the CCD efficiency of the LBCB (left) and LBCR (right). LBCB has the more blue sensitive curve. The dashed line shows the atmospheric absorption at the observatory site. The red lines correspond to the effective filter transmission curves, corrected for CCD efficiency and atmospheric absorption.

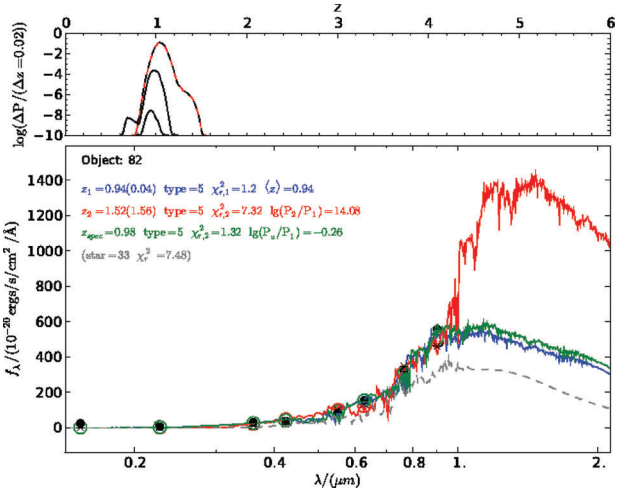

Figure 11. Redshift probability distribution (upper panel) and photometric redshift fit (lower panel) of the spectroscopic object 82, the BCG with $z_{\rm spec} = 0.9786$. The different SEDs are colour coded, the open circles represent the SED integrated within the various filter transmission curves, whereas the black dots represent the measured fluxes. The redshift for the best-fitting SED is $z_{\rm phot} = 0.94 \pm 0.04$, which is in agreement with the spectroscopic one.

of the object relative to the SED model, and from a prior describing the probability for the existence of an object with the given SED type and the derived absolute magnitude as a function of redshift. The code has been successfully applied on the MUNICS survey (Drory et al. 2004), the FORS Deep Field (Gabasch et al. 2004a, 2006), the COSMOS (Gabasch et al. 2008), the *Chandra Deep Field* (Gabasch et al. 2004b) and the CFHTLS (Brimioulle et al. 2008).

Small uncertainties in the photometric zero-point and an imperfect knowledge of the filter transmission curve (see Fig. 9) have to be corrected. We use the colours of stars from the Pickles (1998) library for these adjustments. We compare the colours for this library of stars with the observed colours and apply zero-point shifts to achieve matching. We fix the *i*-band filter and shift the remaining ones by $-0.12, 0.02, 0.01, -0.15$ and 0.10 for the *U*-, *B*-, *V*-, *r*- and *z*-band filters. With additional spectroscopic information we can improve the calibration for the photometric redshift code by slightly adjusting the zero-point offsets for each band again. The match of our observed colours after zero-point shift to the Pickles (1998) stellar library colours is shown in Fig. 10. In Fig. 11 we show the redshift probability distribution of the BCG.

Using all position matchable spectra (31) leads to an accuracy of $\sigma_{\Delta z/(1+z)} = 0.074$ and the fraction of catastrophic outliers is ∼13 per cent, as plotted in Fig. 12. The dotted lines are for $z_{\rm phot} = z_{\rm spec} \pm 0.15(1 + z_{\rm spec})$. The fraction of catastrophic outliers is defined as $\eta = |z_{\rm spec} - z_{\rm phot}|/(1 + z_{\rm spec}) > 0.15$. $\sigma_{\Delta z/(1+z)}$ is the redshift accuracy measured with the normalized median absolute deviation, $1.48 \times {\rm median}(|\Delta z|/(1 + z))$. Using only the secure spectra (17) which fulfil the quality criteria Flag ≥ 3 (≥ 95 per cent confidence; see Paper I) the accuracy becomes $\sigma_{\Delta z/(1+z)} = 0.042$ with no catastrophic outliers.

In Fig. 13, the galaxy redshift histogram of all objects in the field is shown. The galaxy redshift distribution can be parametrized following Van Waerbeke et al. (2001):

$$n(z_{\rm s}) = \frac{\beta}{z_0 \Gamma\left(\frac{1+\alpha}{\beta}\right)} \left(\frac{z_{\rm s}}{z_0}\right)^{\alpha} \exp\left[-\left(\frac{z_{\rm s}}{z_0}\right)^{\beta}\right], \qquad (2)$$

where (z_0, α, β) are free parameters. The best-fitting values for the cluster field are $z_0 = 0.77$, $\alpha = 1.0$ and $\beta = 1.6$. For the fit, we have

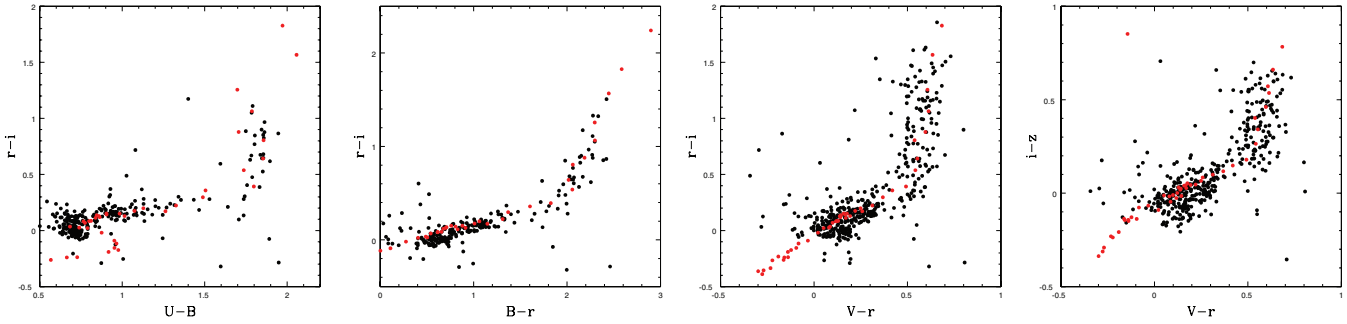

Figure 10. Colour–colour diagrams of stars (black dots), plotted against the Pickles (1998) stellar library (red dots). The stars used in this plot are selected with 17.0 < mag < 23.0 in all bands. The photometric errors (as shown in Fig. 7) are of the order of 0.02 mag. All colours perform well. To obtain these colour–colour diagrams we have applied zero-point corrections to all the bands, in detail −0.12, 0.02, 0.01, −0.15, 0.00 and 0.10 mag for *U, B, V, r, i* and *z* bands.

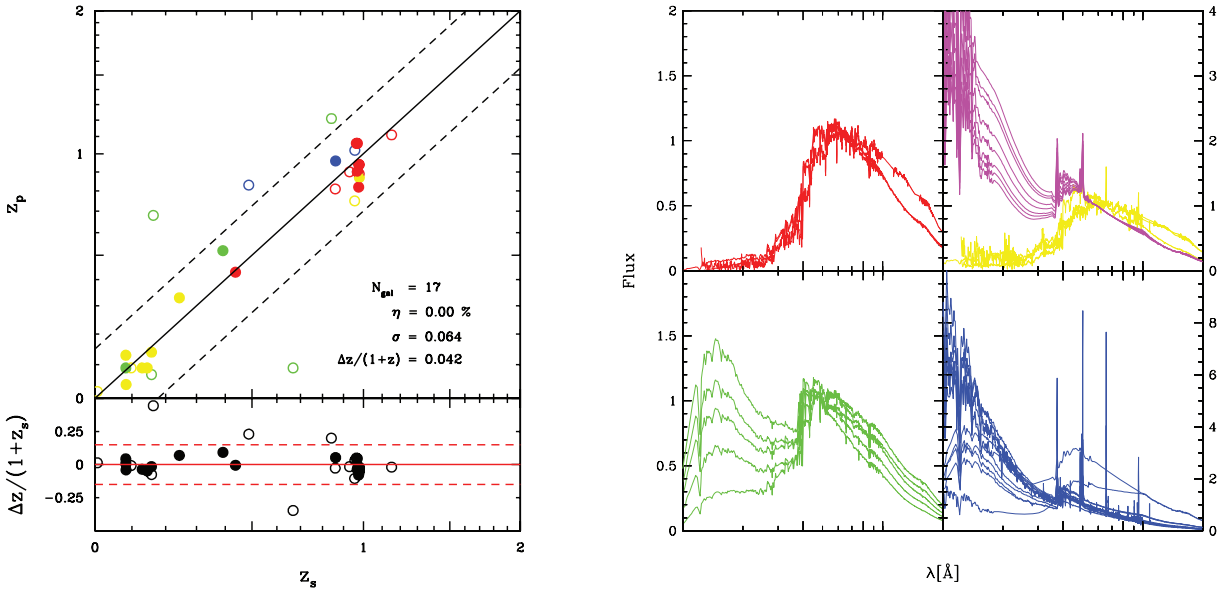

Figure 12. Photometric redshifts, plotted against the spectroscopic ones for the cluster field around XMMU J1230.3+1339. To distinguish the galaxy spectral types (see SED template plotted in the right-hand panel) we use a colour-code: red dots represent ETG (e.g. ellipticals, E/S0), yellow, magenta and green dots represent spiral-like galaxy types (e.g. Sa/Sb,Sbc/Sc) and blue dots represent strong star-forming galaxies (e.g. Sm/Im & SBm). The median residual is $(z_{\rm phot} - z_{\rm spec})/(1 + z_{\rm spec}) = 0.042$, $\sigma_{\Delta z/(1+z)} = 0.074$ and $\eta = 0$ per cent for all secure matchable spectra of the cluster XMMU J1230.3+1339. Note that the filled circle mark secure spectroscopic redshifts.

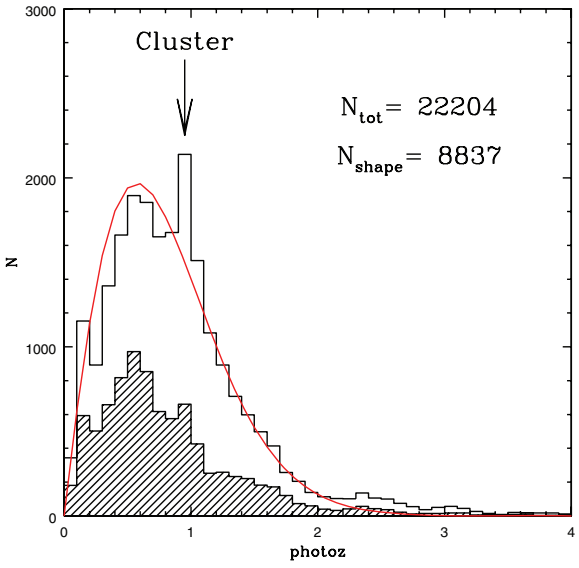

Figure 13. Redshift number distribution of all galaxies. The number distribution is shown as black histogram for the 26 × 26 arcmin^2 field, with a median redshift $z_{\rm median} = 0.77$. The solid red curve represents a fit to the galaxy distribution, using the approach of Van Warbeke et al. (2001). The arrow indicates the galaxy cluster. The shaded distribution shows the objects used for weak lensing analysis later on. These are all objects for which photo-z and shape could be measured within an FOV 26 × 26 arcmin^2 and outside the masked area of Fig. 8.

replaced the peak at $z = 1$ by the average value of the lower and higher bin around the cluster. The fit is shown in Fig. 13.

Since the number of spectroscopic data for this field is still limited we use another method to estimate the photometric redshift accuracy: we measure the two-point angular-redshift correlation of galaxies in photometric redshift slices with $14.0 < i_{AB} < 26.0$ selected from the total sample as shown in Fig. 13, and show the results in Fig. 14. In this way, the null hypothesis of non-overlapping redshift slices can be tested (see Erben et al. 2009; Benjamin et al. 2010 for a detailed description of this technique). For the calculation of the two-point correlation function we use the publically available code ATHENA.[16] The blue curves in Fig. 14 show the autocorrelation of each redshift-bin. The red data points show the cross-correlation of different redshift slices, which should be compatible with zero in the absence of photometric redshift errors. The redshift binning starts from 0 and increases with a stepsize of 0.1 up to redshift 1.0, and stepsize of 0.5 from redshift 1.0 to redshift 4. Nearly all cross-correlation functions of non-neighbouring photo-z slices show indeed an amplitude consistent with or very close to zero. This is a strong argument for the robustness of the photometric redshifts. No excessive overlap between low- and high-z slices is observed. The weak signal in the high-redshift slice is due to the poor statistics in this and the neighbouring bins. Note that the last two bins contain less than 200 galaxies each. For the weak lensing analysis (Section 4) the vast majority of galaxies studied is limited to $z = [1.0–2.5]$. The correlation of all redshift intervals with galaxies in $z\epsilon$ [1.0–2.5] is very small.

3.3 Light distribution

To quantify the light distribution we compute the absolute K-band luminosity for all the galaxies. Based on the SED fitting, performed during the photo-z estimation, we estimate for a given filter curve (K-band) the flux and the absolute magnitude. Next, we map the flux of all galaxies of the cluster in a redshift interval $z_{\rm cluster} \pm 0.05$ on a pixel grid, and smooth it with a circular 2 arcmin Gaussian filter.

[16] www2.iap.fr/users/kilbinge/athena/

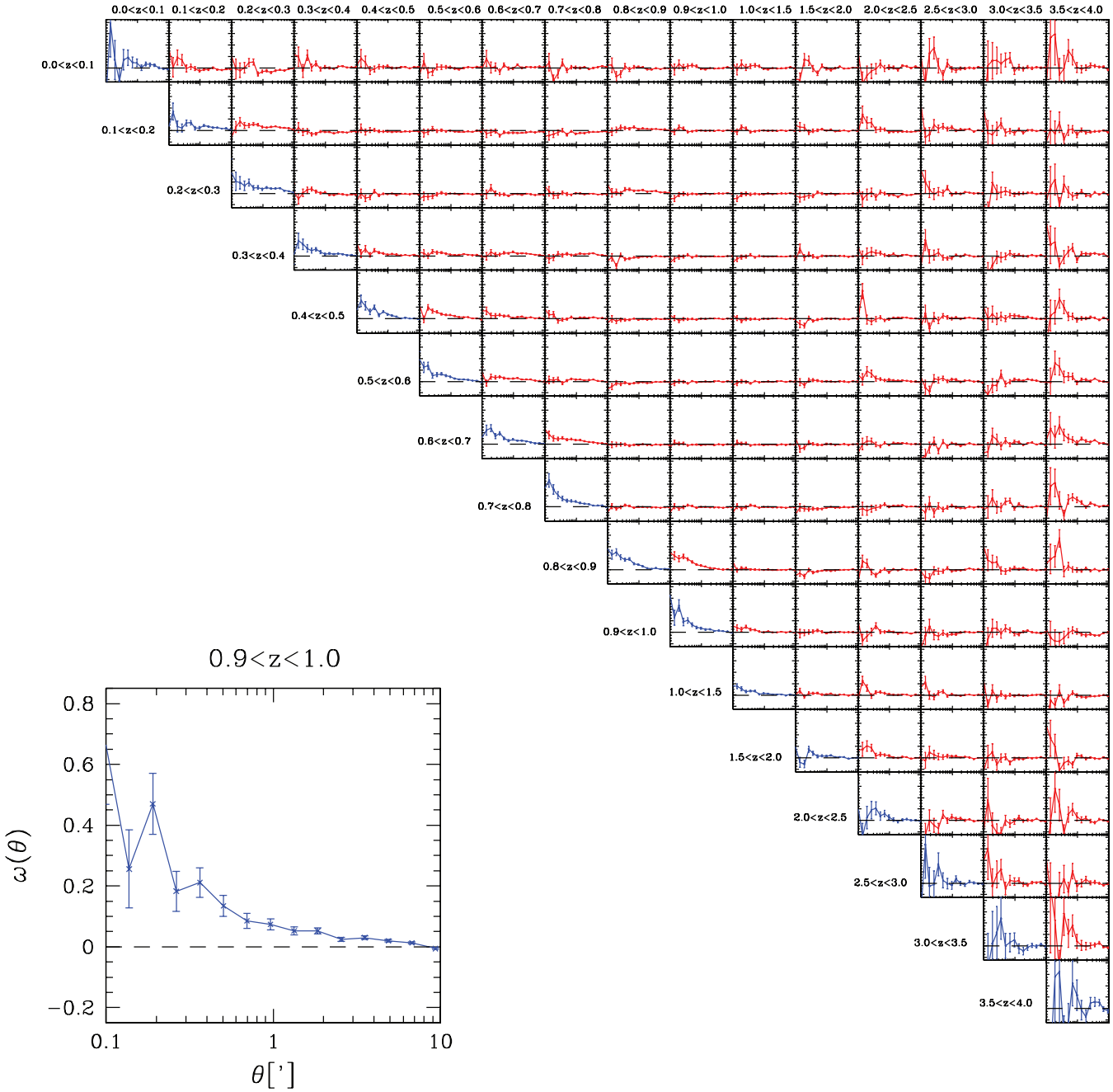

Figure 14. Two-point angular-redshift correlation of galaxies in the field of the cluster XMMU J1230.3+1339 with $14.0 < i_{AB} < 26.0$ selected from the total sample as shown in Fig. 13. The inlay shows as an example the auto-correlation for the redshift bin $0.9 < z_{\rm phot} < 1.0$; the scale of the angular distance is logarithmic from 0.1 to 10 arcmin, whereas the correlation function scales linearly from −0.25 to 0.85. The blue curves show the auto-correlation of each redshift bin. The redshift bins start from 0 and increase by a step-size of 0.1 until redshift 1.0 and step-size of 0.5 from redshift 1.0 to 4. The red curves show the cross-correlation of galaxy subsample pairs at different redshifts.

Fig. 1 shows an LBT image of XMMU J1230.3+1339 with surface brightness contours overlaid. The cluster seems to be very massive, rich and has a lot of substructure (see also Paper I).

3.4 Colour–magnitude relation

The CMR (Visvanathan & Sandage 1977) is a fundamental scaling relation used to investigate the evolution of galaxy populations. The CMR of local galaxy clusters shows a red sequence (RS, Gladders & Yee 2000) formed of massive red elliptical galaxies undergoing passive evolution. For the following discussion, we consider as cluster member those galaxies in a redshift interval $z_{\rm cluster} \pm 0.05$, within a box of 6×6 arcmin^2 centred on the X-ray centroid of the cluster. Our sample is neither spectroscopic nor does it use the statistical background subtraction as it is done when purely photometric sample are studied. As shown in De Lucia et al. (2007) for the ESO Distant Cluster Survey (EDisCS), results are not significantly affected whether one does use spectroscopic or photometric redshifts or does not apply photometric redshifts for member selection. Note that the accuracy of our photometric redshifts is better

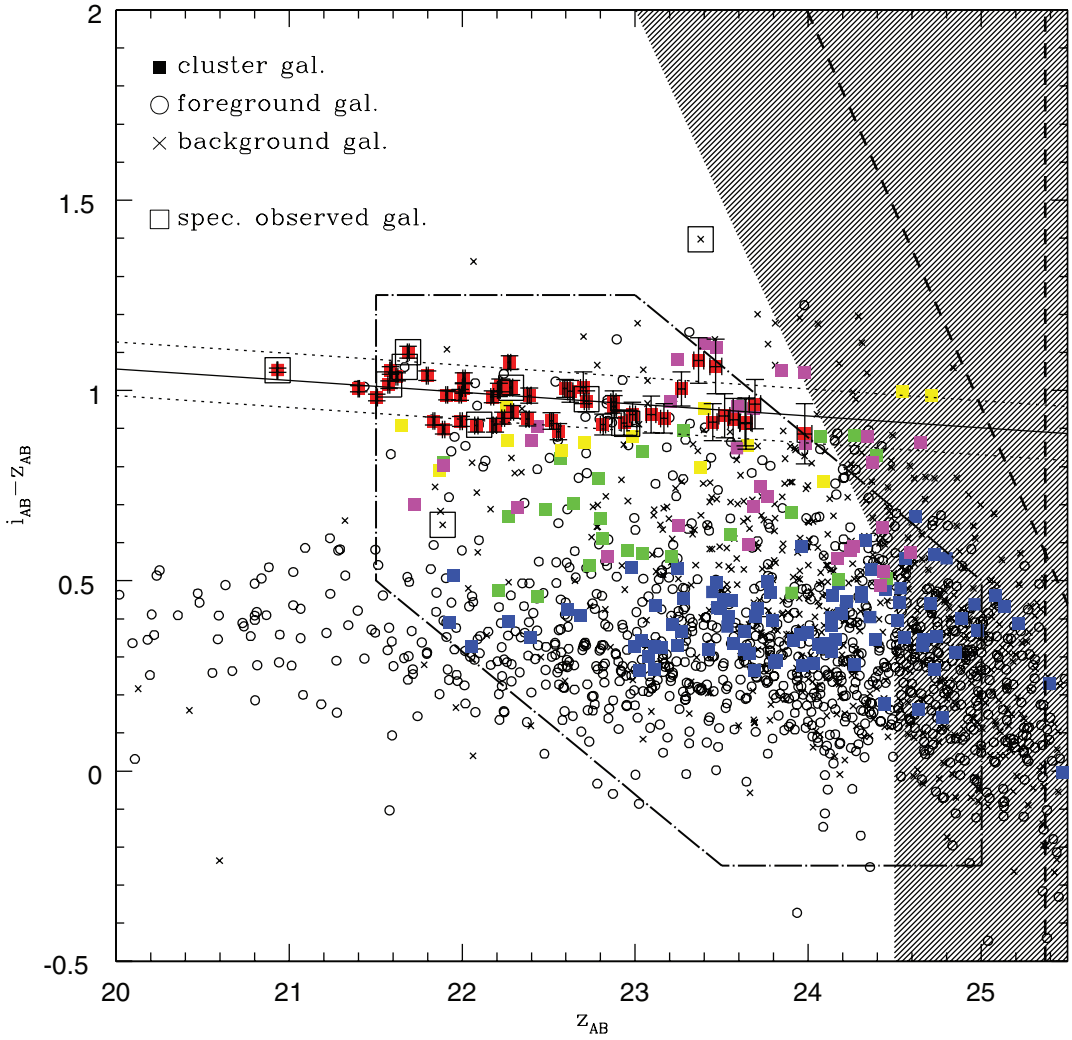

Figure 15. CMR, $i_{AB} - z_{AB}$ against z_{AB}, FOV 6 × 6 arcmin^2, the dashed lines show the 5σ limiting magnitudes and colours. The cluster members are selected to lie at $z_{\rm cluster} - 0.05 \leq z_{\rm phot} \leq z_{\rm cluster} + 0.05$. We use the same colour coding as shown in Fig. 12. The black solid line refers to the linear fit to the passive cluster members, reproduced with red dots. The dotted lines correspond to the 3σ region. The shaded region on the right indicates >50 per cent incompleteness for a point source within a 2 arcsec aperture, which is roughly equal the 50 per cent completeness for an extended galaxy. Black boxes mark spectroscopically confirmed cluster galaxies. The dash–dotted limited region marks the area where we select background galaxies for the WL analysis.

by a factor of 1.5 than those used for EDisCS (see details in Pello et al. 2009; White et al. 2005). This is due to the fact that we can use deep eight-band data (*FUV*, *NUV*, *U*, *B*, *V*, *r*, *i*, *z*) in contrast to five-band data (*V*, *R*, *I*, *J*, *Ks*) for EDisCS.

The CMR for XMMU J1230.3+1339 is shown in Fig. 15. To distinguish the cluster galaxy spectral types we use a colour-code: red dots represent early-type galaxies (ETG; e.g. ellipticals, E/S0), yellow and green dots represent spiral-like galaxy types (e.g. Sa/Sb,Sbc/Sc) and blue dots represent strongly star-forming galaxies (e.g. Sm/Im and SBm).

The CMR shows a tight RS of ETG. The expected colour for composite stellar population (CSP) models with old age and short e-folding time scales or of old single stellar populations (SSP) is $i_{AB} - z_{AB} \approx 1.0$ (e.g. see Santos et al. 2009; Demarco et al. 2007). We apply a linear fit to the nine spectroscopic confirmed RS members at $z_{AB} < 24$ and obtain $i - z = (-0.078 \pm 0.031) \times (z - 24) + 0.849 \pm 0.065$, a result with poor statistics due to the limited number of spectroscopic data. Therefore, we also perform a fit to the 49 photo-z RS members at $z_{AB} < 24$ and obtain $i - z = (-0.0273 \pm 0.012) \times (z - 24) + 0.935 \pm 0.015$. We take the best-fitting RS for the photo-z RS members and plot it in Fig. 15. The slope is consistent in the errors with that obtained by Santos et al. (2009) for XMMU J1229+0151, the 'twin brother' cluster at the same redshift observed with ACS onboard the *Hubble Space Telescope* (*HST*).

We can observe spiral and star-forming galaxies (yellow, green, blue data points) until $z_{AB} = 25.5$. The ETG (red data points) can only by detected until $z_{AB} = 24$. Note that the 50 per cent completeness in z band is 24.5 mag and in i band is 25 mag, which is the detection band. We observe seven galaxies with $23.4 \leq z \leq 23.8$. If the slope of the luminosity function (LF) is $\alpha \approx -1$ we expect about 10 galaxies with $23.8 \leq z \leq 24.2$. We observe only one in this interval. To explore whether this lack of red galaxies is only apparent, caused by incompleteness of red galaxy detection, we have plotted ≤50 per cent completeness region for the i and z detection as a shaded area in Fig. 15. We estimate the detection efficiency of galaxies with $23.8 \leq z \leq 24.2$ and $i - z \approx 1$ to be ≈50 per cent. Hence, we expect to detect about five galaxies against the only one found with $23.8 \leq z \leq 24.2$. Furthermore, we plot the absolute

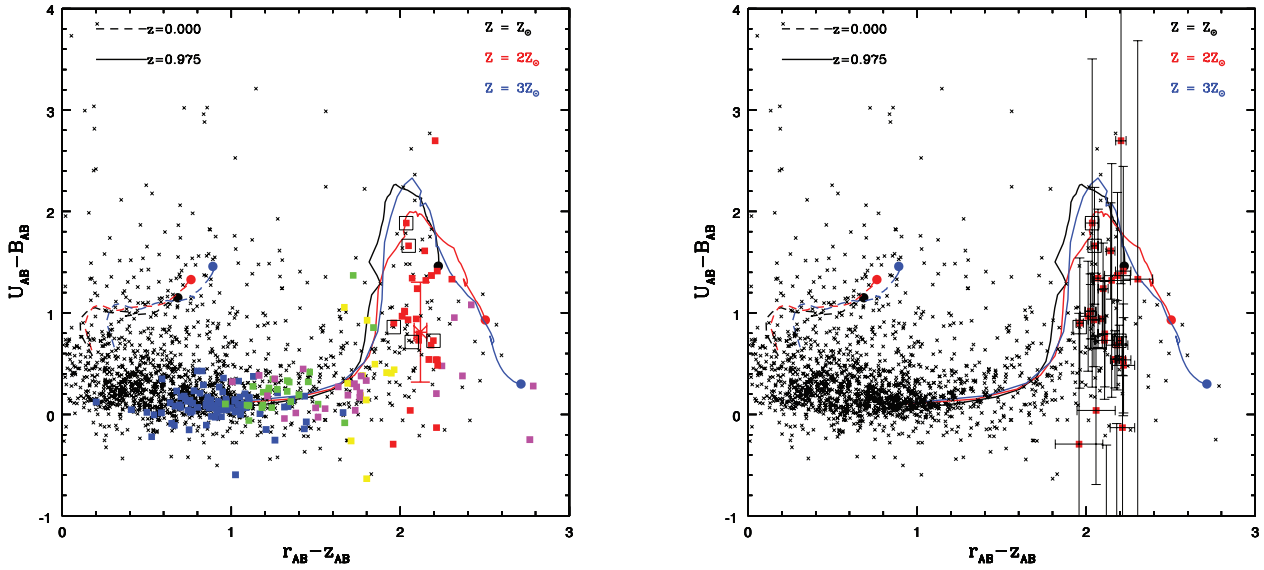

Figure 16. Colour–colour diagram with $U_{AB} - B_{AB}$ against $r_{AB} - z_{AB}$. The same FOV, photometric redshift selection and colour coding as in Fig. 15 are used. On the right-hand panel we show the colour-errors for the ETG. Overplotted we show SSP models for passively evolving galaxies with Salpeter-like IMF and for three different metallicities (one, two and three times solar). The tracks show the time evolution from 100 Myr (filled circles) to 6 Gyr in steps of 100 Myr for two redshifts (0.0 and 0.975). Black boxes in both figures mark spectroscopically confirmed cluster galaxies.

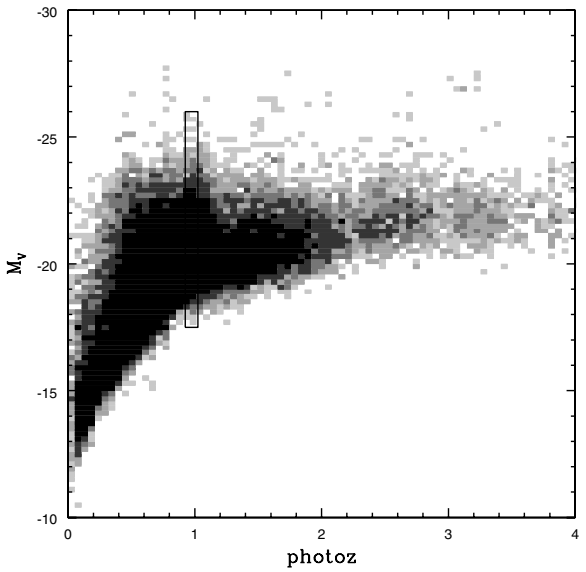

Figure 17. Absolute V-band magnitudes of galaxies in the observed 26 × 26 arcmin^2 field as a function of redshift. The black box shows the region for the selection of cluster members later on.

V-band as a function of redshift in Fig. 17 and the number counts of all cluster galaxies and the ETG ones only as a function of z band and absolute V-band magnitudes in Fig. 18. We can see that ETGs are less and less starting at $z = 22.5$ mag, for which the data are 100 per cent complete. A similar trend can be seen in the absolute V-band magnitude counts, where ETGs with $M_V < -23.5$ become rare. Similar results have been reported for the EDisCS clusters in De Lucia et al. (2007) and the cluster RDCSJ 0910+54 at $z = 1.1$ (Tanaka et al. 2008). Demarco et al. (2007) report an indication for truncation of the $i_{775} - z_{850}$ versus z_{850} CMR (see fig. 15 in Demarco et al. 2007) at a magnitude of $z_{850} = 24.5$ for RDCSJ 1252.9+2927 at $z = 1.24$. A similar trend at $z_{850} = 24.0$ can be seen in fig. 8 of Santos et al. (2009) for XMMU J1229+0151 at $z = 0.975$.

3.5 Blue galaxy fraction – Butcher & Oemler effect

The fraction of blue galaxy types increases from locally a few per cent, 25 per cent ($z = 0.4$) to 40 per cent ($z \sim 0.8$) (see e.g. Schade 1997). This is called the Butcher & Oemler effect.

Butcher & Oemler (1978) defined as blue galaxies those which are by at least $\triangle = 0.2$ mag bluer in the $B - V$ rest frame ($i - z$ observer-frame) than ETG in the cluster. They then counted red galaxies down to an absolute magnitude $M_V = -19.3$ mag within an arbitrary reference radius and applied a statistical subtraction of the background. In contrast to Butcher & Oemler (1984) we use a redshift/SED selection as defined in the previous section. Note that it has been shown by De et al. (2007) that a photometric redshift selection does not affect the result. As seen in Fig. 19 the cluster shows a bimodal galaxy population. The dashed lines in Fig. 19 mark the selection boundaries if one would follow exactly the work of Butcher & Oemler. The colour coding of the galaxy types is shown in Fig. 19. We can infer from our photometric analysis a fraction of blue galaxies $f_b = 0.514 \pm 0.13$ for the cluster and $f_b = 0.545 \pm 0.04$ for the field at the same redshift, with Poisson errors. Note that for the estimate of the fraction of blue galaxies in the field we take the full 26 × 26 arcmin^2 FOV into account and exclude the region around the cluster (6 × 6 arcmin^2).

Our result is in good agreement with the prediction from literature. This can be seen if one extrapolates the blue fraction estimated for the EDisDS sample from $z \approx 0.8$ to $z = 1$ in De Lucia et al. (2007). Within the framework of a state-of-the-art semi-analytic galaxy formation model, Menci et al. (2008) derived an equal fraction of blue galaxies for the cluster and the field at $z \sim 1$.

3.6 Colour–colour diagram

We now turn our attention to the colour–colour diagram of the galaxies. In Fig. 16 we show $r - z$ against $U - B$ colours and overlaid SSP models[17] for passively evolving galaxies with Salpeter-like

[17] Models computed using PEGASE2 (Fioc & Rocca-Volmerange 1997).

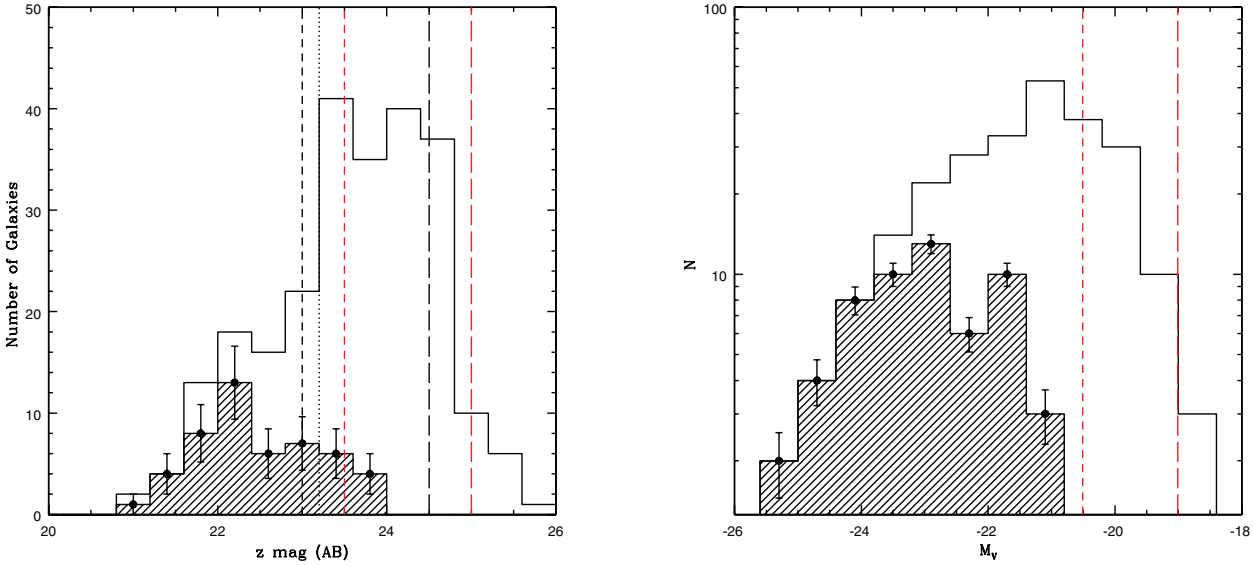

Figure 18. Number counts for the galaxies within a 6 × 6 arcmin^2 region centred on XMMU J1230.3+1339 and a photometric redshift of $z_{\rm cluster} - 0.05 \leq z_{\rm phot} \leq z_{\rm cluster} + 0.05$. The open and shaded histograms show all cluster galaxies and early-type cluster galaxies, respectively. Error bars represent the Poisson errors. The red short (long-dashed) line represents the 100 (50) per cent completeness in the i filter, the detection band and for comparison in black the z filter. The dotted line represents $m(z) \approx 23$, at which galaxies are classified into 'luminous' and 'faint'. There is a rarity of red galaxies with $z \geq 22.2$ or $i \geq 23.2$ or $M_V \geq -24.2$ where the detection efficiency is still 100 per cent in both bands.

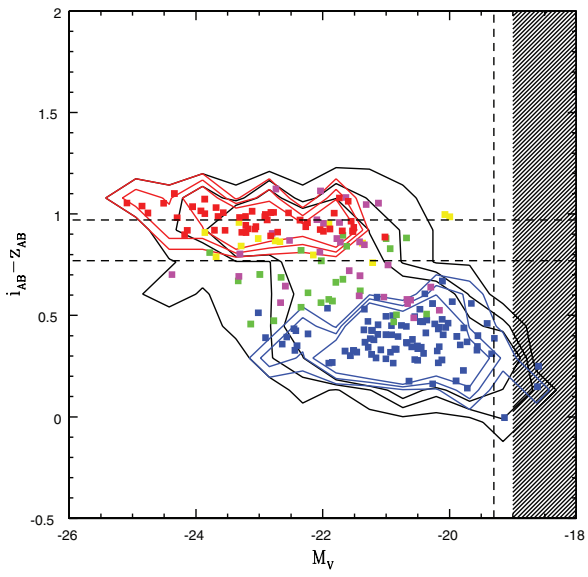

Figure 19. The Butcher & Oemler effect in the CMR, $i_{AB} - z_{ab}$ against $M_{\rm V}$. The dashed lines show the selection box used by Butcher & Oemler (1984) – see text for details. We use the same region, redshift selection and colour coding as in Fig. 15. The contours are colour coded: black lines represent all photometric redshift selected cluster members, and red and blue contours represent the early and late-type cluster population, respectively.

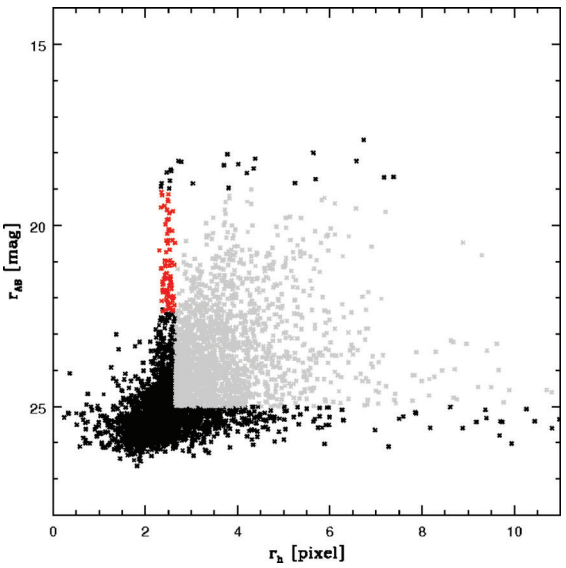

Figure 20. The r-band magnitude versus half-light radius. The red zone shows unsaturated stars selected for the PSF anisotropy correction ($19 < r_{AB} < 22.5$ mag, $2.1 < r_{\rm h} < 2.6$ pixel), where one pixel equals 0.224 arcsec.

IMF and for three different metallicities (one, two and three times solar). We expect a $U_{AB} - B_{AB}$ colour of ≈1.5 from old SSP models with solar metallicity (see tracks in Fig. 16). The colour–colour diagram shows $U_{AB} - B_{AB}$ values from −0.5 to 2.5 in the distribution of the elliptical galaxies (red objects in Fig. 16). Note that the $U_{AB} - B_{AB}$ colours are affected by large U-band measurements errors (see Fig. 7). Nevertheless, we estimate the weighted mean of all ETG in the cluster, which results in a mean colour of $U_{AB} - B_{AB} = 0.81 \pm 0.5$. This could be a mild indication for a recent star formation (SF) episode. The observed $U - B$ colour of a galaxy at $z \sim 1$ corresponds to a rest-frame far-UV colour. It may be no surprise that ETG at this redshift exhibits a rest-frame far-UV colour about 0.8 mag bluer than expected from an SSP model. In fact, at least 30 per cent of the ETG in the local Universe seem to have formed 1–3 per cent of their stellar mass within the previous Gyr (Kaviraj et al. 2007). Hence, it is plausible that a larger fraction of the stellar mass of an ETG at $z \sim 1$ is formed within a look-back time of 1 Gyr. This would produce significantly bluer far-UV colours in the rest frame if attenuation by internal dust is negligible. Alternatively, such bluer colours may spot the presence of a significant UV upturn phenomenon (see Yi 2008, for a review). We will investigate the

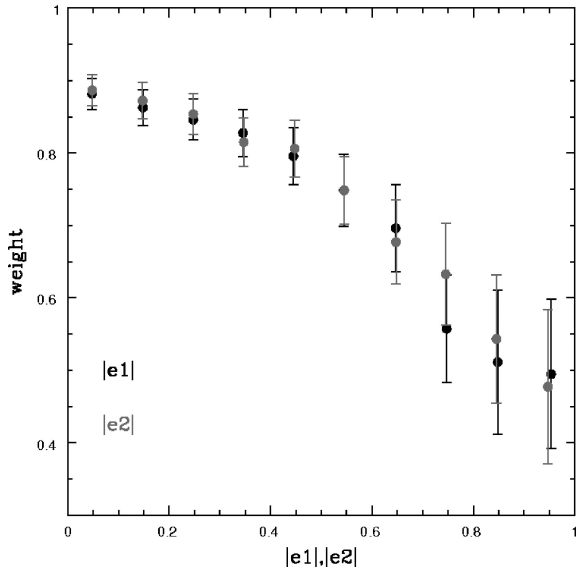

Figure 21. Galaxy weight (see equation 8) as a function of the absolute first and second components of the ellipticity for the weak lensing measurement.

nature of the bluer rest-frame UV colours in ETG in clusters at $z \leq 1$ in a future paper.

4 WEAK LENSING ANALYSIS

In this section, we give an overview on the applied shape measurement technique and on the lensing mass estimators; we use standard lensing notation. For a broad overview to the topic, see e.g. Mellier (1999), Bartelmann & Schneider (2001) and Hoekstra & Jain (2008).

4.1 Gravitational shear estimate with the KSB method

The ellipticity of a background galaxy provides an estimate of the trace-free components of the tidal field $\partial^2\psi/\partial\theta_i\partial\theta_j$, where $\psi(\theta)$ is the two-dimensional potential generated by the surface density $\kappa(\theta)$ (Kaiser & Squires 1993) of the mass distribution of the cluster. Any weak lensing measurement relies on the accurate measurement of the average distortion of the shape of background galaxies. Therefore, it is crucial to correct for systematic effects, in particular for asymmetric contributions to the PSF from the telescope and from the atmosphere.

The most common technique is the so-called KSB method proposed by Kaiser, Squires & Broadhurst (1995) and Luppino & Kaiser (1997). In the KSB approach, for each source the following quantities are computed from the second brightness moments

$$Q_{ij} = \int \mathrm{d}^2\theta\, W_{r_\mathrm{g}}(|\theta|)\theta_i\theta_j I(\theta), \quad i, j \in \{1, 2\}, \tag{3}$$

where W_{r_g} is a circular Gaussian weight function with filter scale r_g,[18] and $I(\theta)$ is the surface brightness distribution of an image:

(1) the observed ellipticity

$$\epsilon = \epsilon_1 + i\epsilon_2 = \frac{Q_{11} - Q_{22} + 2iQ_{12}}{Q_{11} + Q_{22}}, \tag{4}$$

(2) the smear polarizability P^sm and (3) the shear polarizability P^sh.

[18] We choose r_g to be equal to the SExtractor parameter FLUX_RADIUS.

The KSB method relies on the assumption that the PSF can be described as the sum of an isotropic component which circularizes the images (seeing) and an anisotropic part introducing a systematic contribution (for a detailed discussion see e.g. Kaiser et al. 1995; Luppino & Kaiser 1997; Hoekstra et al. 1998, hereafter KSB+).

The source ellipticity ϵ^s of a galaxy after PSF smearing (Bartelmann & Schneider 2001) is related to the observed one, ϵ, and to the reduced shear g by

$$\epsilon_i - \epsilon_i^s = P_{ij}^g g_j + P_{ij}^\mathrm{sm} p_j^*, \tag{5}$$

where the anisotropy kernel p describes the effect of the PSF anisotropy (an asterisk indicates that the parameters are derived from the measurement of stars):

$$p_i^* = (P^{\mathrm{sm}*})_{ij}^{-1}\epsilon_j^*. \tag{6}$$

The p quantity changes with the position across the image, therefore it is necessary to fit it by, e.g., a third-order polynomial, so that it can be extrapolated to the position of any galaxy. The term P^g, introduced by Luppino & Kaiser (1997) as the pre-seeing shear polarizability, describes the effect of the seeing and is defined as

$$P_{ij}^g = P_{ij}^\mathrm{sm}\left(\frac{P_{ij}^\mathrm{sh}}{P_{ij}^\mathrm{sm}} - \frac{P_{im}^{\mathrm{sh}*}}{P_{mj}^{\mathrm{sm}*}}\right), \tag{7}$$

with the shear and smear polarizability tensors P^sh and P^sm, calculated from higher-order brightness moments as detailed in Hoekstra et al. (1998). In Fig. 22, we plot the distribution of the values of half-light radius r_h and r_{AB} magnitude of the galaxies used later on for our weak lensing analysis. The computed $P^\mathrm{sh}/P^\mathrm{sm}$ values for different bins of r_h and r_{AB} are shown in Fig. 23.

Following Hoekstra et al. (1998), the quantity $P^{\mathrm{sh}*}/P^{\mathrm{sm}*}$ should be computed with the same weight function used for the galaxy to be corrected. The weights on ellipticities are computed according to Hoekstra et al. (2000),

$$w = \frac{1}{\sigma_g^2} = \frac{(P^g)^2}{(P^g)^2\sigma_{\epsilon_0}^2 + \langle\Delta\epsilon^2\rangle}, \tag{8}$$

where $\sigma_{\epsilon_0} \sim 0.3$ is the scatter due to intrinsic ellipticity of the galaxies, and $\langle\Delta\epsilon^2\rangle^{1/2}$ is the uncertainty on the measured ellipticity. In Fig. 21, we show the galaxy weight as a function of the absolute first and second components of the ellipticity.

We define the anisotropy-corrected ellipticity as

$$e_i^\mathrm{ani} = e_i - P_{ij}^\mathrm{sm} p_j^*, \tag{9}$$

and the fully corrected ellipticity ϵ^iso as

$$e_i^\mathrm{iso} = \frac{1}{P_{ij}^g} e_j^\mathrm{ani}, \tag{10}$$

which is an unbiased estimator for the reduced gravitational shear

$$\langle\epsilon_\mathrm{iso}\rangle = g = g_1 + ig_2 = \frac{\gamma}{1-\kappa}, \tag{11}$$

assuming a random orientation of the intrinsic ellipticity. For the weak distortions measured, $\kappa \ll 1$, and hence

$$\langle\epsilon_\mathrm{iso}\rangle = g. \tag{12}$$

Our KSB+ implementation uses a modified version of Nick Kaiser's IMCAT tools, adapted from the 'TS' pipeline (see Heymans et al. 2006; Schrabback et al. 2007), which is based on the Erben et al. (2001) code. In particular, our implementation interpolates between pixel positions for the calculation of Q_{ij}, P^sm and P^sh and measures all stellar quantities needed for the correction of the galaxy

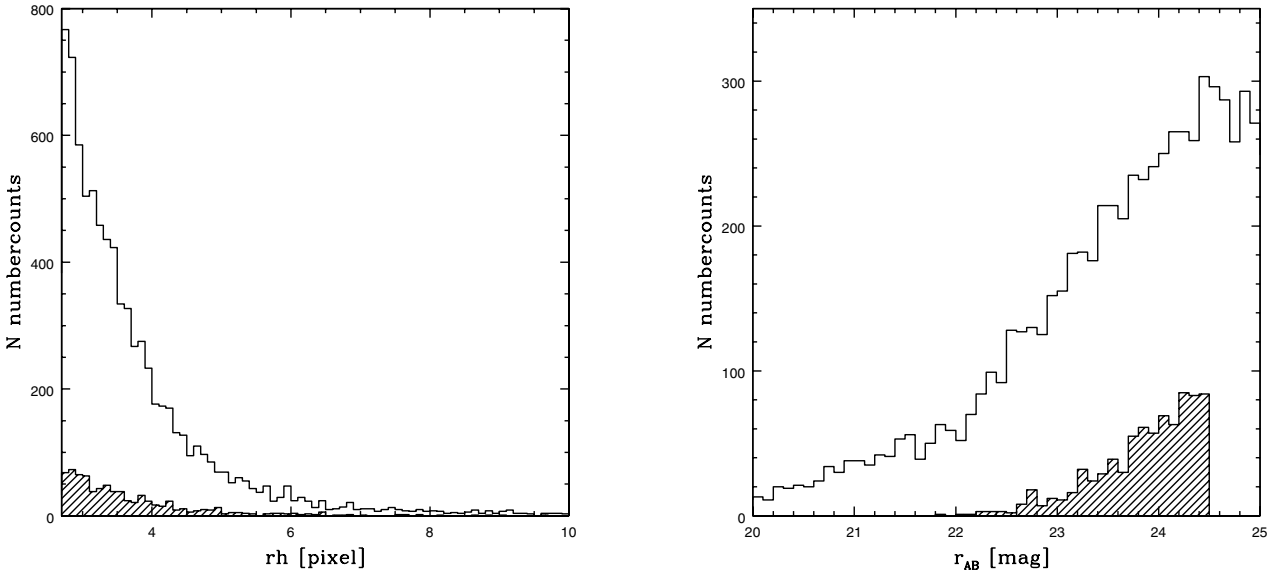

Figure 22. Distribution of the r_h and r_{AB} magnitude values of all galaxies used for the weak lensing analysis. The shaded distribution shows the 785 objects used to perform the weak lensing study on XMMU J1230.3+1339.

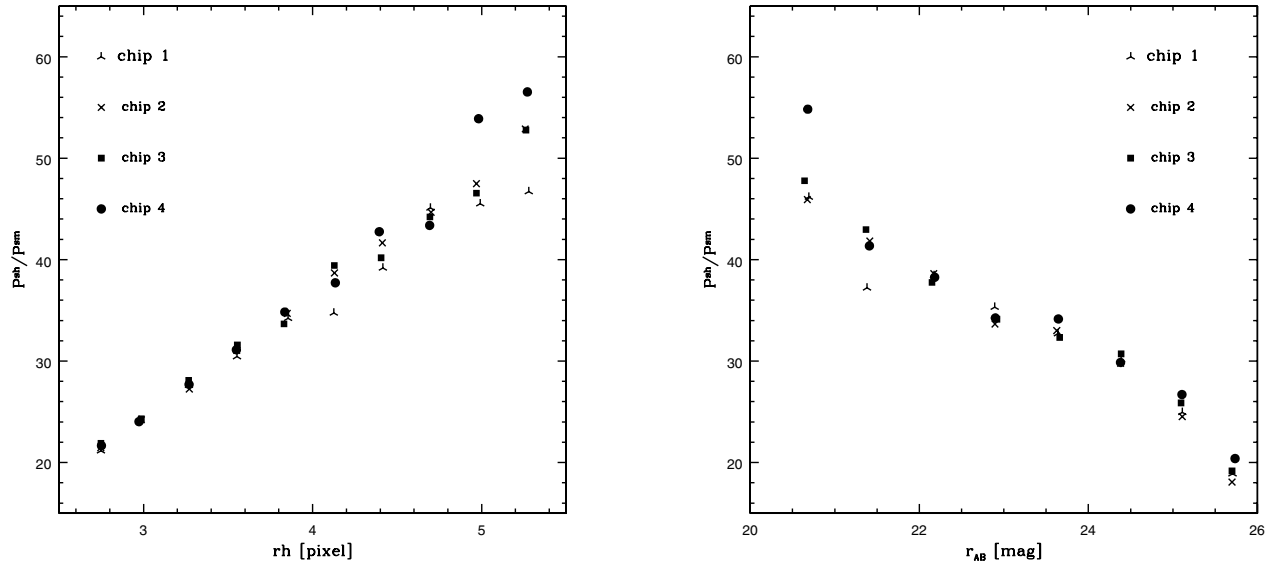

Figure 23. PSF correction: P_{sh}/P_{sm} values of all galaxies used for the weak lensing analysis computed in different bins of r_h and r_{AB} magnitude and for each chip.

ellipticities as a function of the filter scale r_g following Hoekstra et al. (1998). This pipeline has been tested with image simulations of the STEP project.[19] In the analysis of the first set of image simulations (STEP1) a significant bias was identified (Heymans et al. 2006), which is usually corrected by the introduction of a shear calibration factor

$$\langle g \rangle = c_{cal} \cdot \langle \epsilon_{iso} \rangle \quad (13)$$

with $c_{cal} = 1/0.91$. In the analysis of the second set of STEP image simulations (STEP2), which takes realistic ground-based PSFs and galaxy morphology into account, it could be seen that with this calibration factor the method is on average accurate to the ∼3 per cent level[20] (Massey et al. 2007).

Note that for the weak lensing analysis we only consider the *r*-band stack. Neither do we use the *i*-band stack, because we observe larger residuals of the anisotropy correction, nor do we make use of the *z*-band stack, which shows remaining fringe patterns after data reduction. We select stars in the range $19 < r_{AB} < 22.5$ mag, $0.48 < r_h < 0.58$ arcsec, giving 322 stars (see Fig. 20) to derive the quantities for the PSF correction. Fig. 24 shows the distortion fields of stellar ellipticities before and after PSF anisotropy correction as a function of their pixel position of the *r*-band stack. The direction of the sticks coincides with the major axis of the PSF; the lengthscale is

[19] http://www.physics.ubc.ca/ heymans/step.html

[20] Note that dependencies of shear on size and magnitude will lead to different uncertainties.

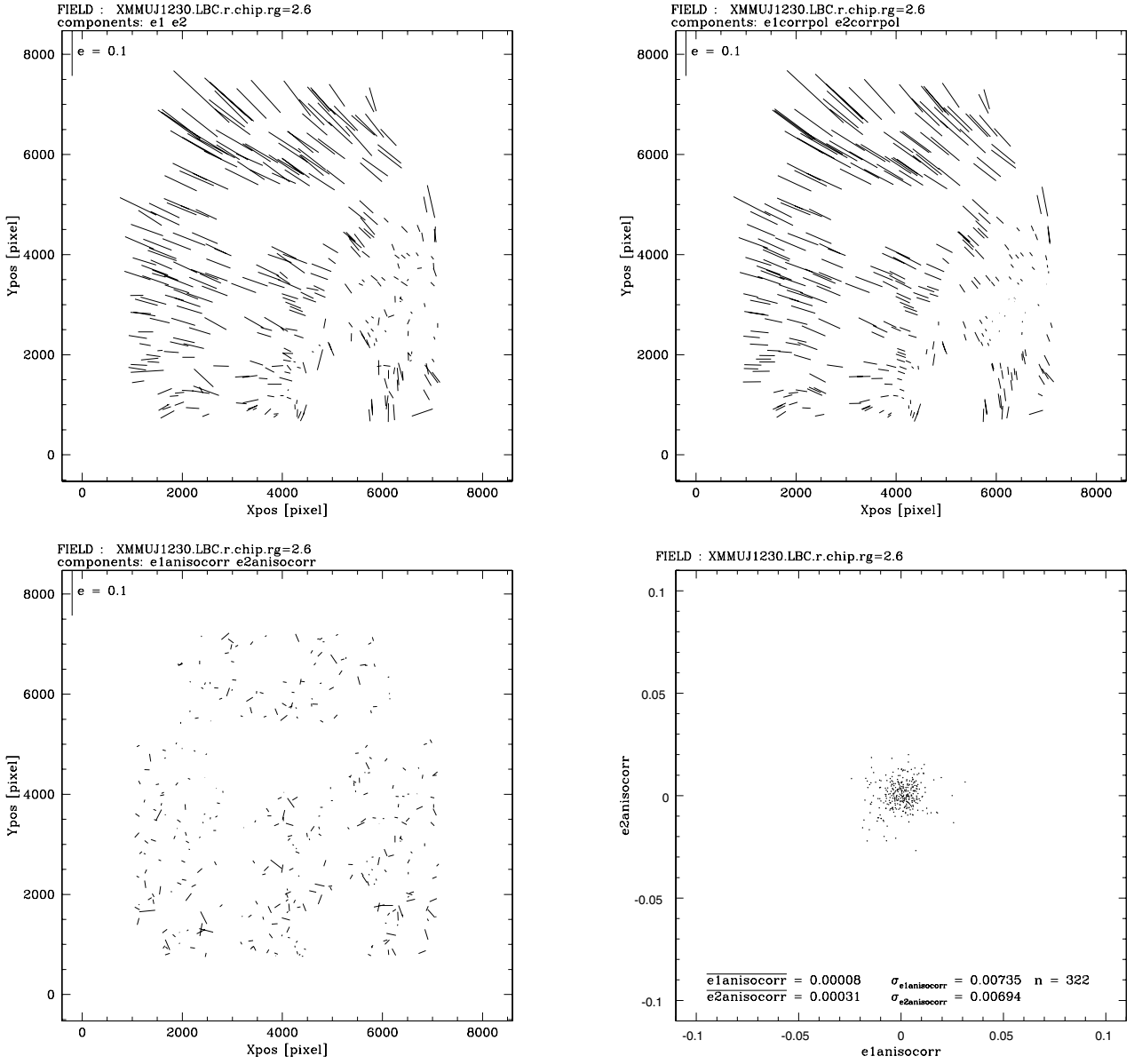

Figure 24. PSF anisotropy correction: ellipticities of the stars in the field of XMMU J1230.3+1339 as observed (top-left panel) and fitted (top-right panel), plus their residuals (bottom-left panel) after correction for PSF anisotropies as a function of their pixel position of the *r*-band stack. The direction of the sticks coincides with the major axis of the PSF; the lengthscale is indicating the degree of anisotropy. An ellipticity of 10 per cent is shown in the upper-left corner of two upper and the bottom-left panel. The definition of ellipticity is given in equation (4). The stars initially had systematic ellipticities up to ∼3–8 per cent in one direction. The PSF correction (bottom-right panel) reduced these effects to typically <1.5 per cent.

indicating the degree of anisotropy. The stars initially had systematic ellipticities up to ∼3–8 per cent in one direction. The PSF correction reduced these effects to typically <1.5 per cent.

Galaxies used for the shear measurement were selected through the following criteria: $w > 3, \mathrm{SNR} > 5, z_{\mathrm{phot}} > 1.03, r_{\mathrm{h}} > 0.58$ arcsec, $r_{AB} < 25.5$ mag and ellipticities, e_{iso}, smaller than one. This yields a total number of 785 background galaxies in the catalogue, and an effective number density of background galaxies ($z_{\mathrm{phot}} > 1.03$) of $n_{\mathrm{eff}} \sim 7$ galaxies per arcmin^2. In Fig. 15 we show the distributions in the $i_{AB} - z_{AB}$ against z_{AB} colour–magnitude diagram of the members of the galaxy cluster XMMU J1230.3+1339 and the background galaxies. The area is limited with the dash–dotted line. Note that without accurate photometric redshifts a separation of background from foreground and cluster member galaxies cannot be achieved.

The measurement of the shape of an individual galaxy provides only a noisy estimate of the weak gravitational lensing signal. We therefore average the measurements of a large number of galaxies as a function of cluster centre distance. Fig. 26 shows the resulting average tangential distortion e_{t} of the smear and anisotropy-corrected galaxy ellipticity as a function of the distance from the X-ray centroid of the galaxy cluster. The error bars on e_{t} and e_{c} indicate Poissonian errors. We detect a significant tangential alignment of galaxies out to a distance of ∼4 arcmin or ∼2 Mpc from the cluster centre. The black points represent the signal e_{c}, when the phase of the distortion is increased by $\pi/4$. If the signal observed is due to

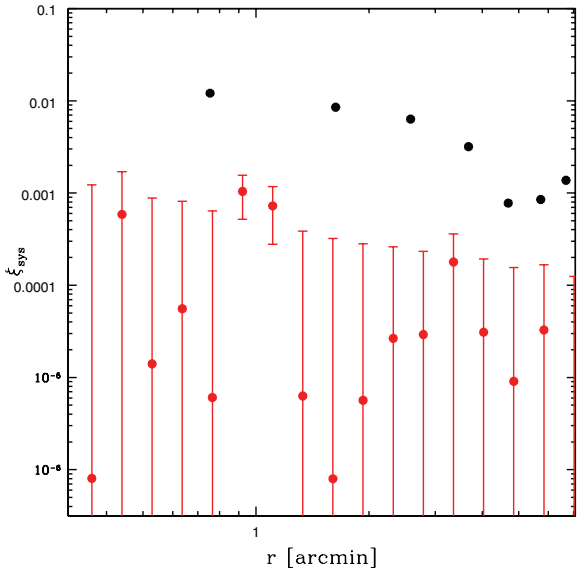

Figure 25. PSF systematic residual: the cross-correlation function $\xi_{\rm sys}$ (red points) between galaxies and stars is shown as a function of angular scale. The amplitude of the cross-correlation is always at least one order of magnitude smaller than the shear signal $\xi_E \sim e_{\rm t}^2$ (black filled).

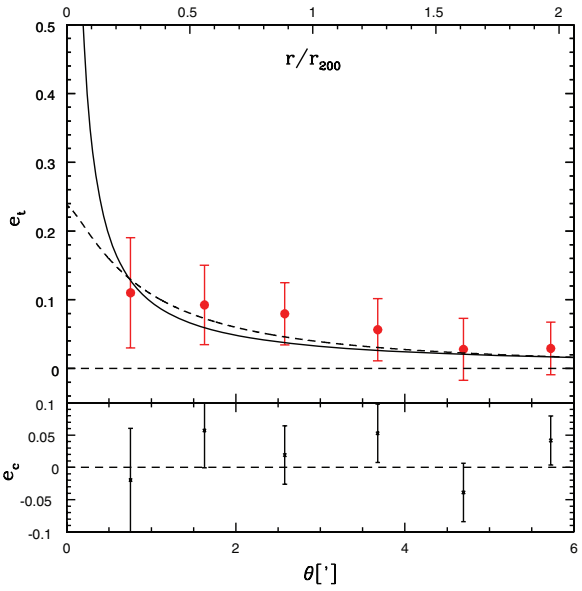

Figure 26. Radial profiles of the tangential shear $\epsilon_{\rm t}$ (in red, measure of the signal) and the cross shear $\epsilon_{\rm c}$ (in black, measure of the systematics) around the cluster XMMU J1230.3+1339. The error bars indicate the statistical error in the measurement, due to the intrinsic ellipticity of the individual sources. The black solid line shows the fit of an SIS model to the data, which yields a velocity dispersion of $\sigma = 1308 \pm 284\,{\rm km\,s^{-1}}$ (χ^2/DOF = 1.66/5), while the dashed line shows the NFW model.

gravitational lensing, $e_{\rm c}$ should vanish, as observed. For distances beyond ∼4 arcmin, the values of the tangential and cross shear are similar, which sets the limit of the present data. To obtain a mass estimate of the cluster, we fit a singular isothermal sphere (SIS) density profile to the observed shear. We use photometric redshifts for the computation of angular distances, where $D_{\rm s}$, $D_{\rm d}$ and $D_{\rm ds}$ are the distances from the observer to the sources, from the observer to the deflecting lens and from the lens to the source. We show our results in Fig. 26, where the solid line is the best-fitting SIS

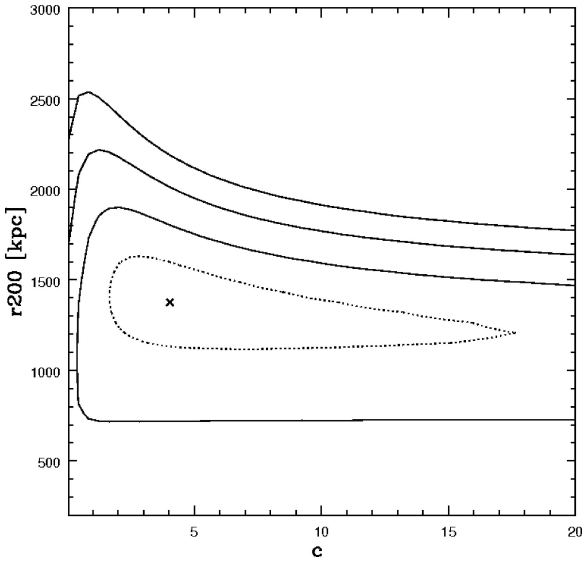

Figure 27. Likelihood confidence contours for the NFW fit to the two shear components on a grid centred on the cluster. The solid line contours are for 1, 2 and 3σ confidence levels (68.3 per cent, 95.4 per cent and 99.73 per cent, respectively) with best-fitting parameters $c = 4.0^{+14}_{-2}$ and $r_{200} = 1376^{+200}_{-228}$ kpc (χ^2/DOF = 1784/783). The dotted line indicates the 50 per cent significance level.

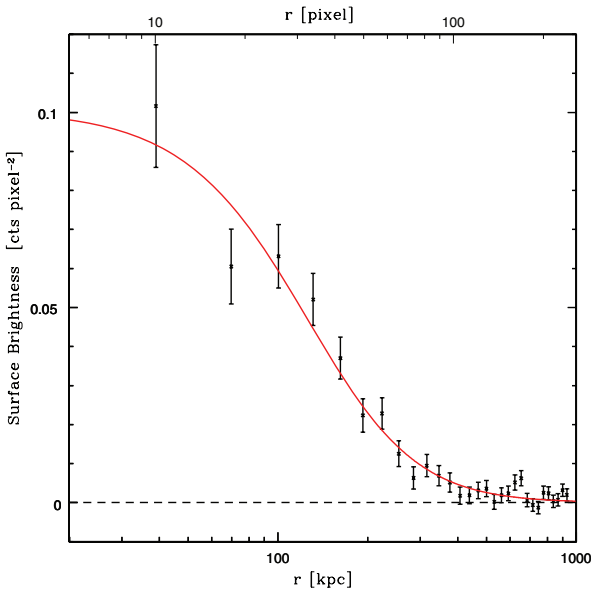

Figure 28. Radial surface brightness profile of XMMU J1230.3+1339 for the 0.29–7.0 keV band sampled in 4 arcsec annular bins (pixel size = 0.492 arcsec pixel^{-1}). The red solid line traces the best-fitting single β model with $r_{\rm c} = 39.99$ pixel ($155\,h_{72}^{-1}$ kpc) and $\beta = 0.67$.

model which yields an equivalent line-of-sight velocity dispersion of $\sigma = 1308 \pm 284\,{\rm km\,s^{-1}}$ and χ^2/DOF = 1.66/5.

In addition to the SIS model considered so far, from now on we use in addition an NFW model (Navarro, Frenk & White 1996; 1997) to describe the density profile of the cluster. This is because an NFW model automatically provides a virial mass M_{200}. An NFW model at redshift z is defined as

$$\rho(r) = \frac{\delta_{\rm c}\rho_{\rm c}}{(r/r_{\rm s})(1 + r/r_{\rm s})^2}, \qquad (14)$$

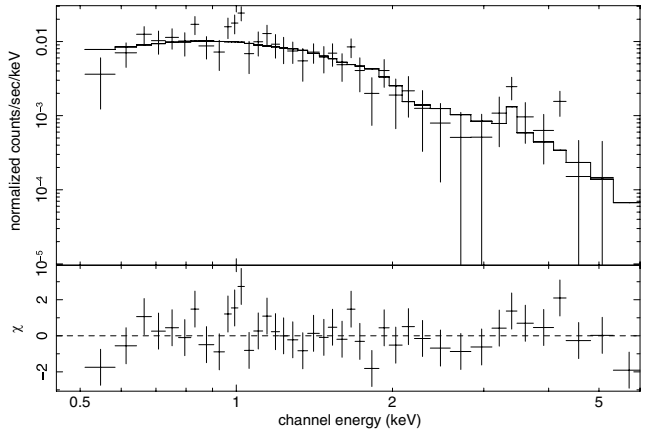

Figure 29. Core spectrum of XMMU J1230.3+1339. The spectrum is fit with a single temperature spectral model, extracted from a circle centred on the emission peak with a radius of 40 arcsec (∼315 kpc) for the 0.5–7 keV band, grouped to include 20 counts per bin. The fit to the minimally binned data resulted in an ambient cluster temperature of 5.29 ± 1.02 keV. The Fe K-line is visible at 3.3 keV.

where

$$\delta_c = \frac{200}{3}\frac{c^3}{\ln(1+c) - c/(1+c)} \tag{15}$$

is the characteristic density, $c = r_{200}/r_s$ is the concentration parameter, r_s is the scale radius and $\rho_c(z) = 3H(z)^2/8\pi G$ is the cosmological critical density. The mass within a radius R is given by

$$M(r \le R) = 4\pi\delta_c\rho_c(z)r_s^3\Big[\ln\Big(1+\frac{R}{r_s}\Big) - \frac{R/r_s}{1+R/r_s}\Big], \tag{16}$$

and the corresponding mass M_{200} is given by

$$M_{200} = 200\rho_c(z)\frac{4\pi}{3}r_{200}^3. \tag{17}$$

We perform a likelihood analysis (see Schneider et al. 2000 for details of the method) to fit an NFW model to the measurements. This yields a concentration parameter of $c = 4^{+14}_{-2}$, a scale radius of $r_s = 345^{+50}_{-56}$ kpc and χ^2/DOF = 1784/783 within a 50 per cent significance interval, as shown in Fig 27.

We test our lensing signal for contamination by the imperfect PSF anisotropy correction. Following Bacon et al. (2003), we compute the correlation between the corrected galaxy and uncorrected stellar ellipticities. To assess the amplitude we normalize the quantity by the star–star uncorrected ellipticity correlation.

$$\xi_{\rm sys}(r) = \frac{\langle e^*(x)\gamma(x+r)\rangle^2}{\langle e^*(x)e^*(x+r)\rangle}, \tag{18}$$

where the 'asterisk' indicates a stellar quantity. In Fig. 25, we show the cross-correlation compared to the shear signal $\xi_E \sim e_t^2$ up to 10 arcmin. Note that the amplitude is at least one order of magnitude smaller than the signal. We conclude that the PSF correction is well controlled.

4.2 Aperture mass $M_{\rm ap}$

We make use of the aperture mass statistics, introduced by Schneider (1996) and worked out further by Schneider & Bartelmann (1997) to quantify the mass density concentration and the signal of the weak lensing detection. The aperture mass statistic has the advantage that it can be derived from the shear field in a finite region and $M_{\rm ap}$ is not influenced by the mass-sheet degeneracy. It is defined as

$$M_{\rm ap}(\theta_0^c) = \int {\rm d}^2\theta\kappa(\theta)U(\theta - \theta_0^c), \tag{19}$$

where $U(\theta)$ is a radially symmetric weight function, using a compensated filter function of radius θ_0^c,

$$\int_0^{\theta_0^c} {\rm d}\theta\theta U(\theta) = 0. \tag{20}$$

One can express $M_{\rm ap}$ in terms of the tangential shear ϵ_t

$$M_{\rm ap}(\theta_0^c) = \int {\rm d}^2\theta\epsilon_t(\theta)Q(|\theta - \theta_0^c|). \tag{21}$$

The filter functions Q and U are related through

$$Q(\theta) = \frac{2}{\theta^2}\int_0^\theta {\rm d}\theta'\theta' U(\theta') - U(\theta). \tag{22}$$

It was shown by Schneider (1996) and Bartelmann & Schneider (2001) that the variance $\sigma_{M_{\rm ap}}$ of $M_{\rm ap}$ and $M_{\rm ap}$ itself can be estimated for observational data in a straightforward way. In fact, one only has to change the integral into a sum over galaxy ellipticities and the error analysis is simply expressed by

$$M_{\rm ap} = \frac{\pi\theta_0^2\sum_i \epsilon_{t,i}w_i Q(|\theta_i - \theta_0^c|)}{\sum_i w_i}, \tag{23}$$

$$\sigma^2_{M_{\rm ap}} = \frac{\pi^2\theta_0^4\sum_i \epsilon_{t,i}^2 w_i^2 Q^2(|\theta_i - \theta_0^c|)}{2(\sum_i w_i)^2}, \tag{24}$$

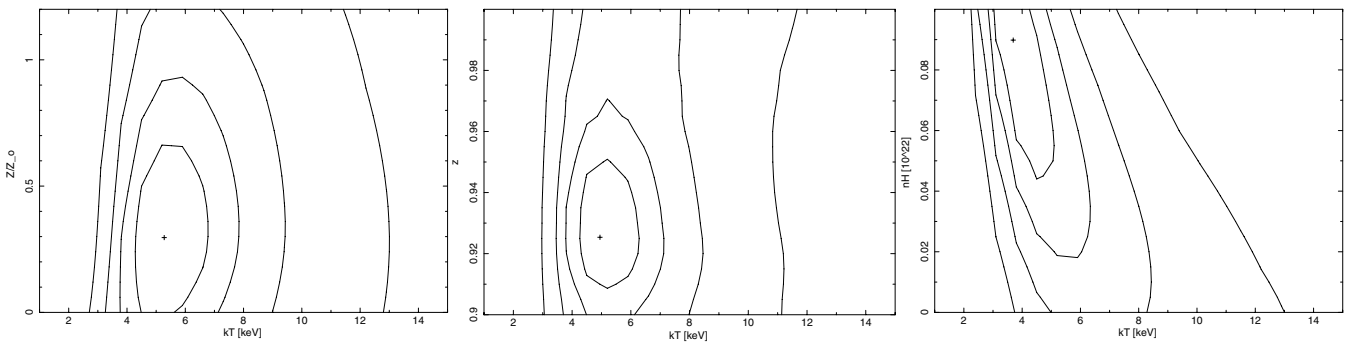

Figure 30. Confidence contours obtained from the spectral fit to the X-ray data for XMMU J1230.3+1339. Best-fitting temperature T and iron abundance $Z/Z_\odot$ (left-hand panel), cluster redshift z (middle panel), and Galactic absorption $N_{\rm H}$ (right-hand panel) are marked as crosses. The solid contours represent 1, 2, 3σ confidence levels.

Table 4. Comparison of different X-ray statistics.

	Cash-stat[a] (minimally binned, $N_{\rm H}$,Z/Z$_\odot$,$z_{\rm cl}$ fixed)	Cash-stat[b] (minimally binned, $N_{\rm H}$,$z_{\rm cl}$ fixed)	χ^2-stat (20 counts bin^{-1}, $N_{\rm H}$,Z/Z$_\odot$, $z_{\rm cl}$ fixed)	χ^2-stat (20 counts bin^{-1}, $N_{\rm H}$,$z_{\rm cl}$ fixed)	χ^2-stat (30 counts bin^{-1}, $N_{\rm H}$,Z/Z$_\odot$,$z_{\rm cl}$ fixed)	χ^2-stat (30 counts bin^{-1}, $N_{\rm H}$,$z_{\rm cl}$ fixed)
$N_{\rm H}$	2.64	2.64	2.64	2.64	2.64	2.64
kT	5.29 ± 1.02	5.28 ± 1.02	4.73 ± 1.12	4.85 ± 1.12	4.75 ± 1.16	4.76 ± 1.17
Z/Z$_\odot$	0.30	0.29 ± 0.24	0.3	0.74 ± 0.43	0.30	0.54 ± 0.43
$z_{\rm cluster}$	0.975	0.975	0.975	0.975	0.975	0.975
C/DOF	486.05/444	486.05/444	–	–	–	–
$\chi^2_{\rm red}$/prob.	–	–	0.72/0.965	0.71/0.969	0.84/0.709	0.86/0.679

[a]Used for the X-ray mass estimate. Galactic absorption $[N_{\rm H}] = [10^{20}\,{\rm cm}^{-2}]$, global temperature $[kT]$ = [keV], solar abundance $[Z/Z_\odot] = [1]$, cluster redshift $[z_{\rm cluster}] = [1]$, likelihood function C/DOF, and min. criterion $\chi^2_{\rm red}$/null hypothesis probability.
[b]Confidence contours are shown in Fig. 30.

Table 5. Mass estimates for XMMU J1230.3+1339.

Reference	r_{200} (kpc)	M_{200} ($10^{14}\,{\rm M}_\odot$)	$M_{r\leq 1\,{\rm Mpc}}$ ($10^{14}\,{\rm M}_\odot$)	Method (remark)
This work	$944 + 397$	$2.85 + 3.6$	$3.01 + 3.8$	Kinematics
This work	1046 ± 113	3.87 ± 1.3	3.72 ± 1.2	X-ray
This work	1376 ± 218	8.80 ± 4.2	6.74 ± 3.3	WL (NFW)[a]
This work	1125 ± 188	4.56 ± 2.3	–	Combination
Paper I	1017 ± 68	4.19 ± 0.7	–	Combination

[a]We use for the r_{200} the 50 per cent significance level.

where $\epsilon_{{\rm t},i}$ are the tangential components of the ellipticities of lensed galaxies relative to each of the grid points investigated, and w_i are the weights defined in equation (8).

Therefore, the S/N can by calculated as

$$\mathrm{S/N} = \frac{M_{\rm ap}}{\sigma_{M_{\rm ap}}}. \tag{25}$$

We use the polynomial filter function introduced by Schneider (1996):

$$Q(\theta) = \frac{6}{\pi}\frac{(\theta/\theta_0^c)^2}{(\theta_0^c)^2}\left(1 - \left(\theta/\theta_0^c\right)^2\right), \tag{26}$$

where θ is the projected angular distance on the sky from the aperture centre, and θ_0^c is the filter radius. We apply this weight function to the data.

We detect a weak lensing signal at a 3.5σ significance. The location of the highest significance coincides with the X-ray measurement of the *Chandra* analysis (see Section 6). In Fig. 1, we show an LBT image of XMMU J1230.3+1339 with $M_{\rm ap}$ S/N-contours overlaid. We observe an elongation in the projected mass distribution from weak lensing in the same direction as the distribution of galaxies associated with the main cluster component and the group bullet (see Paper I), and the X-ray emission.

5 KINEMATIC ANALYSIS

For the cluster kinematic analysis, the redshifts and positions of galaxies are used to define a characteristic velocity dispersion and a characteristic size (scale radius) of the cluster. According to the virial theorem, the RMS velocity dispersion has the property to be completely independent of any shape and viewing angle (see Carlberg et al. 1996).

5.1 RMS velocity dispersion

Following Carlberg, Yee & Ellingson (1997) the line-of-sight velocity dispersion is defined as

$$\sigma_{\rm v}^2 = \frac{\sum_i w_i v_{{\rm pec}_i}^2}{\sum_i w_i}, \tag{27}$$

where w_i are magnitude-dependent geometric weights,

$$v_{{\rm pec}_i} = \frac{c(z_i - \bar{z}_{\rm cl})}{1 + \bar{z}_{\rm cl}}, \tag{28}$$

the peculiar velocity in the frame of the cluster, and $z_{\rm cl}$ is the mean redshift of the cluster.

An alternative approach (Carlberg et al. 1997) is the unweighted line-of-sight velocity dispersion, defined as

$$\sigma_{\rm v}^2 = \frac{\sum_i v_{{\rm pec}_i}^2}{N - 1}. \tag{29}$$

For a virial mass estimator the projected mean harmonic pointwise separation can be used as

$$\frac{1}{R_{\rm H}} = \sum_{i\leq j}\frac{w_i w_j}{|r_i - r_j|}\Big(\sum_i w_i\Big)^{-2}, \tag{30}$$

where *ij* indicates a sum over all pairs. The three-dimensional virial radius is defined as

$$r_{\rm vir} = \frac{\pi R_{\rm H}}{2}. \tag{31}$$

The virial mass of the cluster is defined as

$$M_{\rm vir} = \frac{3\sigma_{\rm v}^2 r_{\rm vir}}{G}. \tag{32}$$

We use the model of a singular, isotropic, isothermal sphere with a velocity dispersion of $\sigma_{\rm SIS} = \sigma_{\rm v}$, and therefore a density profile of

$$\rho(r) = \frac{\sigma_{\rm v}^2}{2\pi G r^2}. \tag{33}$$

To compare masses usually an extrapolation to a constant mean interior density of $200\rho_{\rm crit}$ is performed, using

$$M_{200} = M_{\rm vir}\sqrt{\frac{\bar{\rho}(r_{\rm vir})}{200\rho_{\rm crit}}}, \tag{34}$$

where the mean density $\bar{\rho}(r_{\rm vir})$ inside $r_{\rm vir}$ is defined as

$$\bar{\rho}(r_{\rm vir}) = \frac{3M_{\rm vir}}{4\pi r_{\rm vir}^3}. \tag{35}$$

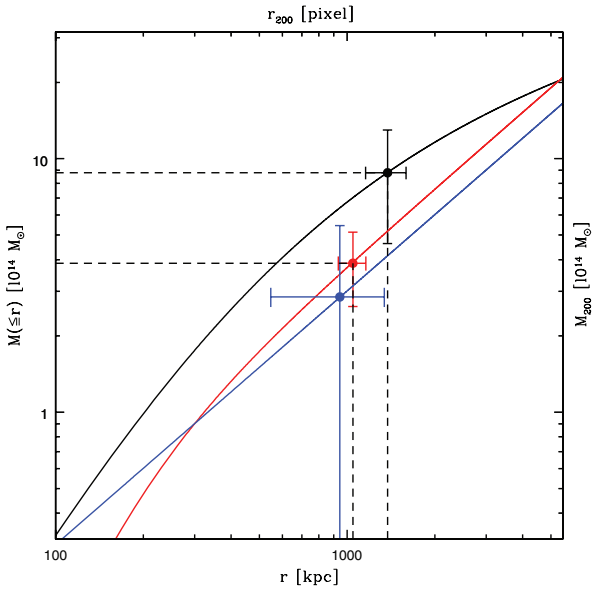

Figure 31. Mass Profile of XMMU J1230.3+1339. In black: best-fittings NFW profile from weak lensing; in blue: best-fitting kinematic SIS profile; in red: best-fitting X-ray β-model profile. We have added the M_{200} and r_{200} values with error bars for each method.

5.2 Cluster membership

Next, we define the cluster membership of galaxies. Generally, this is determined in two ways.

5.2.1 3σ clipping technique

The statistical clipping technique (e.g. Zabludoff, Huchra & Geller 1990) is a method to identify cluster members. It is based on the measured recession velocities of the galaxies. Yahil & Vidal (1977) showed that this is a reasonable assumption, if the velocity distribution of the galaxies follows a Gaussian distribution and clusters are relaxed and isothermal.

5.2.2 Mass model method

Another technique to assess the boundaries of a cluster under usage of the spatial and redshift data is the mass model method (Carlberg et al. 1997). We make use of the model described in Pimbblet et al. (2006) for the Las Campanas Observatory and Anglo-Australian Telescope Rich Cluster Survey (LARCS), which is based on Carlberg et al. (1996).

For our kinematic mass estimate we use the line-of-sight velocity dispersion $\sigma_{\rm SIS}^{\rm los} = 657 \pm 277\,{\rm km\,s^{-1}}$, compiled in Paper I.

Based on the assumption that a cluster is a SIS (Carlberg et al. 1997),

$$r_{200} = \frac{\sigma_{\rm v}}{10H(z)}, \tag{36}$$

where $\sigma_{\rm v} \approx \sqrt{3}\sigma_{\rm SIS}^{\rm los}$ is the velocity dispersion of the cluster and $H(z)^2 = {\rm H}_0^2[\Omega_{\rm M}(1+z)^3 + \Omega_{\rm k}(1+z)^2 + \Omega_\Lambda]$. We estimate $r_{200} = 944 + 397\,{\rm kpc}$ and $M_{200} = (2.85 + 3.60) \times 10^{14}\,{\rm M}_\odot$; note that due to the poor statistics we only give upper limits. We would need more spectroscopic data of cluster members to improve the estimate together with its uncertainty.

6 X-RAY ANALYSIS

6.1 Surface brightness profile

A radial surface brightness profile was computed from a combined, point-source-removed image and exposure map over the range 0.29–7.0 keV in 4 arcsec annular bins, using the CIAO 4.1 tools DMEXTRACT and DMCALC.

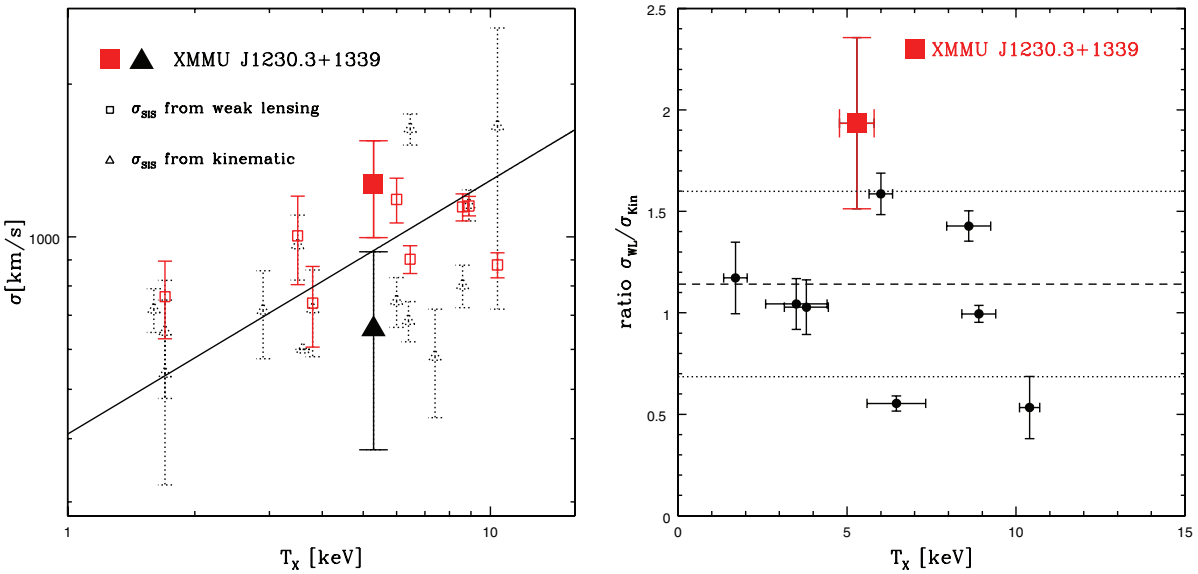

Figure 32. Temperature, $T_{\rm X}$, and galaxy velocity dispersion, σ, relation for distant ($z > 0.8$) galaxy clusters (left-hand panel). Velocity dispersions and temperatures are taken from Table C1. The solid line shows the relation $k_B T_{\rm X} = \mu m_{\rm p} \sigma^2$ (e.g. see Böhringer et al. 2010b; Rosati, Borgani & Norman 2002). Red open boxes (black dotted triangles) mark galaxy velocity dispersions taken from weak lensing (kinematic) analyses. XMMU J1230.3+1339 with $T_{\rm X} = 5.3 \pm 1\,{\rm keV}$ and $\sigma = 1308 \pm 284\,{\rm km\,s^{-1}}$ is represented as large filled red box. Ratio, $\sigma_{\rm WL}/\sigma_{\rm Kin}$, of the velocity dispersion form the weak lensing and the kinematic analysis against temperature $T_{\rm X}$ (right-hand panel) for the nine distant ($z > 0.8$) galaxy clusters taken from Table B1. The mean average ratio is 1.14 $\pm$ 0.46.

The surface brightness profile was then fitted with a single β model (Cavaliere & Fusco-Femiano 1976) of the form:

$$I(r) = I_0 \left(1 + \frac{r^2}{r_c^2}\right)^{-3\beta+\frac{1}{2}}, \quad (37)$$

where I_0 is the normalization, r_c is the core radius and β can be determined from the profile at $r \gg r_c$.

The best-fitting β model of this cluster is described by $r_c = 39.99 \pm 12.58$ pixel ($155 \pm 46.5\, h_{72}^{-1}$ kpc), $\beta = 0.67 \pm 0.20$ (see Fig. 28). The reduced χ^2 of the fit was 1.20 for 27 degrees of freedom.

6.2 Global temperature

Using the X-ray centroid position indicated in Section 2.4.1, a point source removed spectrum was extracted from the observation in a circular region with a 40 arcsec ($315\, h_{72}^{-1}$ kpc) radius. The spectrum was then analysed in XSPEC 11.3.2 (Arnaud 1996), using weighted response matrices (RMF) and effective area files (ARF) generated with the CIAO 4.1 tools SPECEXTRACT, MKACISRMF, MKWARF and the *Chandra* calibration data base version 4.1. The background was extracted from the aimpoint chip in regions free from the cluster emission. The resulting spectrum, after background subtraction, extracted from the observation contains 639 source counts. The spectrum is fitted with a single temperature spectral model (MEKAL; see Mewe, Gronenschild & van den Oord 1985; Mewe, Lemen & van den Oord 1986; Kaastra 1992; Liedahl, Osterheld & Goldstein 1995) including Galactic absorption, as shown in Fig. A1. The absorbing column was fixed at its measured value of 2.64×10^{20} cm^{-2} (Dickey & Lockman 1990), and the metal abundance was fixed at 0.3 solar (Edge & Stewart 1991). Data with energies below 0.5 keV and above 7.0 keV were excluded from the fit.

The best-fitting temperature of the spectrum extracted from within this region was $T_X = 5.29 \pm 1.02$ keV, with a Cash-statistic $C = 486.05$ for 444 degrees of freedom. Using this spectrum, the unabsorbed luminosity of XMMU J1230.3+1339 within 40 arcsec ($315\, h_{72}^{-1}$ kpc) radius is $L_X = 1.48 \times 10^{44}$ erg s^{-1} (0.5–2.0 keV). In Fig. 29, we show a plot of the spectrum with the best-fitting model overlaid. The spectrum was grouped to include at least 20 counts per bin. We performed several tests in order to assess the robustness of our results against systematics by changing background regions and by using different statistics. A comparison of the Cash-statistic and χ^2-statistic is shown in Table 4; the best-fitting temperature varies by only ~10 per cent. The impact of a possible calibration problem of ACIS-S at high energies has been alleviated by using the latest calibration files.

The resulting temperature, combined with the density profile inferred from the β model fit

$$\rho_{gas}(r) = \rho_0 \left[1 + \frac{r^2}{r_c^2}\right]^{-3\beta/2}, \quad (38)$$

and the mass equation derived from hydrostatic equilibrium

$$M_{tot}(< r) = -\frac{kT(r)r}{G\mu m_p} \left(\frac{\delta \ln \rho}{\delta \ln r} + \frac{\delta \ln T}{\delta \ln r}\right), \quad (39)$$

(where μm_p is the mean mass per particle), were then used to estimate the value of r_{200}, following Ettori (2000)

$$r_{200} = r_c \sqrt{\left[\frac{3\beta kT}{G\mu m_p (4/3)\pi \rho_c(z) r_c^2 200}\right] - 1}, \quad (40)$$

where r_c is the core radius. With $\mu = 0.62$, we obtain $r_{200} = 1046 \pm 113$ kpc. The total mass is then calculated out to r_{200}, using the equation

$$M_{tot}(< r) = \frac{3\beta}{G} \frac{kTr}{\mu m_p} \frac{(r/r_c)^2}{1 + (r/r_c)^2}. \quad (41)$$

7 CLUSTER MASS ESTIMATES

In this section, we compare the masses determined with different methods, namely from the kinematics of the cluster galaxies, X-ray emission of the cluster gas and weak lensing.

As seen from Table 5, the mass estimates from the NFW fit, kinematics and X-ray analyses are in good agreement within the error bars. In Fig. 31, we plot the mass estimates against the corresponding radius. The dynamical mass estimate is on the low side but still consistent with the other measurements due to the low statistics.

8 DISCUSSION

Here, we discuss the results of our optical, weak lensing, kinematic and X-ray analyses and compare XMMU J1230.3+1339 to other high-redshift clusters (see e.g. Appendix, Table C1). A more general discussion of the global cluster properties (e.g. mass proxies, scaling relations, large-scale structure) can be found in Paper I.

8.1 Colour–magnitude relation

We observe evidence for a deficit of faint red galaxies, down to a magnitude of $z_{AB} = 24.5$ (50 per cent completeness), based on our photo-z/SED classification (see Figs 15 and 18). Similar results have been reported for several clusters at $z = 0.7$–0.8, for RXJ0152 by Tanaka et al. (2005), for RXJ1716 by Koyama et al. (2007) and for 18 EDisCS clusters by De Lucia et al. (2007), and for RDCSJ 0910+54 at $z = 1.1$ by Tanaka et al. (2008). However, there are other clusters still under debate, like e.g. MS 1054, where Andreon (2006) showed the faint end of the CMR and in contrast to that Goto et al. (2005), who measured a deficit at 1σ level for the same cluster. Some other known clusters seem to have their faint end of the CMR in place, like the eight clusters between redshifts 0.8 and 1.27 studied in detail by Mei et al. (2009) and also the 'twin' cluster XMMU J1229+0151 at $z = 0.975$ (Santos et al. 2009).

Koyama et al. (2007) suggested to collect more observations to study the deficit of faint red galaxies, since it can be seen only in the richest clusters and therefore a larger cluster sample is necessary.

XMMU J1230.3+1339 is a very rich, massive, high-redshift cluster, and this may have some impact on the build-up of the CMR. We will explore the build-up of the CMR in clusters at $z \leq 1$ and do a comparison with semi-analytical modelling of hierarchical structure and galaxy formation in an upcoming paper.

8.2 Blue galaxy fraction – Butcher & Oemler effect

About half of the cluster members have a blue galaxy type, as inferred from the photo-z/redshift classification. This is in good agreement with the prediction of De et al. (2007), Menci et al. (2008) and Haines et al. (2009): an increase in the fraction of blue galaxies with increasing redshift.

Note that the photometric redshift estimates for blue galaxies are usually worse than those for red galaxies, due to the different shape of the SEDs (see right-hand panel of Fig. 11 for details) which results in larger uncertainties. This cannot be seen in this data set, because we only have 'red' spectroscopic clusters members (see

Ilbert et al. 2006; Brimioulle et al. 2008 for the dependence of photometric redshift accuracy on different SED types and magnitude intervals). The larger photometric redshift errors of blue galaxies lead to an underestimation of the blue galaxy fraction due to an increased scattering of object into neighbouring redshift bins [see e.g. the small signal bins $z = (0.8–0.9)$ and $z = (1.0–1.5)$ in Fig. 14].

8.3 Colour–colour diagram

Focusing on the colour-coded cluster members, based on the photo-z/SED classification one can easily see that a separation between foreground and background for the blue galaxies is hardly possible without knowing the redshift. The SSP models, computed using PEGASE2 (Fioc & Rocca-Volmerange 1997), nicely reproduce the observed colours of the ETG of the cluster and the field. Note that when observing a cluster at redshift ∼1, the flux of the cluster members in the blue bands is very low, especially in the U band, therefore the measurement errors are large.

For example, additional NIR observations (J and K bands down to $J^* + 4$ and $K_s^* + 5$) can reveal the existence of an additional intermediate-age stellar population, and constrain the star formation rate (SFR) of all cluster members together with the available data. With these data we will also be able to study slope, scatter and zero-point of the RS in the $J - K$ CMR. To further understand the evolution of cluster elliptical galaxies around $z = 1$ not only the strength of the 4000 Å break is essential, but also the measurement of the fraction of young and intermediate stellar populations is essential.

8.4 Mass estimates

8.4.1 Weak lensing analysis

Very recently, Romano et al. (2010) performed the first weak lensing study using the LBT. They analysed the galaxy cluster Abell 611 at $z \sim 0.3$ and demonstrated that the LBT is indeed a suitable instrument for conducting weak lensing studies. We observe a weak lensing signal for a cluster at a redshift of $z \sim 1$, the most distant cluster so far used in a ground-based weak lensing study. We were able to derive a weak lensing mass estimate for the following reasons.

(1) Deep high-quality multiband data (U, B, V, r, i, z) have been taken under subarcsec seeing conditions in order to resolve faint, small and distant objects (cluster members and background galaxies).

(2) We obtained accurate photometric redshifts and SED classifications to separate cluster members, foreground and background galaxies. This avoids a dilution of the shear signal from cluster member and foreground galaxies, which would lead to an additional mass uncertainty of ∼4 per cent (see Hoekstra 2007).
A conventional background separation using the CMR or colour–colour diagram is not possible (see e.g. Medezinski et al. 2010) since the background galaxies are not distinguishable from cluster members and foreground galaxies in the colour–magnitude or colour–colour space.

(3) The PSF pattern was stable and isotropic over the entire observation time, and could be modelled with a fifth-order polynomial. The systematic error is almost 1/3 of the signal for angular scales considered in the weak lensing analysis.

We had to reject on average one-third of the available data (in each band) to produce the stacked images for our scientific exploitation (see Section 2.1 for details). Note that our method (KSB) to measure galaxy shapes and extract the shear signal is similar to the one applied in Romano et al. (2010).

We used spectroscopic data and the two-point angular-redshift correlation analysis to investigate the photometric redshift accuracy. The PSF systematic residual has been tested with the cross-correlation function between galaxies and stars. All tests perform very well, and we conclude that the systematics are minimal. We derive a velocity dispersion of $\sigma_{\rm SIS}^{\rm WL} = 1308 \pm 284\,{\rm km\,s^{-1}}$ by fitting an SIS model to the tangential shear profile. From the NFW likelihood analysis, we find a best-fitting concentration parameter $c = 4.0^{+14}_{-2}$ and a scale radius $r_{\rm s} = 344^{+50}_{-57}\,{\rm kpc}$. The concentration parameter is only weakly constrained. Nevertheless, the best-fitting value is in good agreement with the relation of Bullock et al. (2001) and Dolag et al. (2004). This results in a total mass of $M_{200}^{\rm NFW} = (8.80 \pm 4.17) \times 10^{14}\,{\rm M}_{\odot}$.

Hoekstra (2003) analysed the effect of the large-scale structure along the line of sight, which also contributes to the lensing signal, and consequently affects the mass estimates. This introduces a factor of ∼3 for the uncertainties in M_{200} and a factor of ∼2 for the concentration parameter c at the redshift of $z = 1$ (extrapolated from fig. 7 in Hoekstra 2003). For deep *HST* observations of MS 1054-0321 ($z = 0.89$), Jee et al. (2005b) estimated an additional ∼14 per cent error for the total cluster mass due to cosmic shear. Our analysis is limited by the large statistical error of the measurement (shape noise), which is the driving uncertainty of our mass estimate.

XMMU J1230.3+1339 is located behind the local Virgo cluster ($z = 0.0038$), which covers a sky area of $8 \times 8\,{\rm deg}^2$, while XMMU J1230.3+1339 covers $6 \times 6\,{\rm arcmin}^2$.

The Virgo cluster acts like a mass sheet, with a constant surface mass density ($\kappa = $ const.) leading to a constant deflection angle ($\alpha = $ const.) and no shear ($\gamma = 0$). Note that the surface mass density κ is indirectly proportional to $\Sigma_{\rm crit}$. The critical surface mass density $\Sigma_{\rm crit}$ depends on the ratio $D_{\rm s}/(D_{\rm d}D_{\rm ds})$ (Schneider 1996), which leads in the case of the Virgo cluster lens geometry to a high value of $\Sigma_{\rm crit}$. Therefore, κ becomes negligibly small for the Virgo cluster.

We observe an elongation in the projected mass distribution from the $M_{\rm ap}$ statistic similar to the distribution of galaxies associated with the main cluster component and the group bullet (see Paper I) and the X-ray emission. Currently, the statistics and the depth are not sufficient to resolve the possible substructure peaks associated with the central group merger event. The WL separation of the main cluster and the group bullet will require high-resolution space-based imaging data.

8.4.2 Kinematic analysis

The current analysis is based on only 13 cluster members, resulting in a total mass of $M_{200}^{\rm Kin} = (2.85 + 3.60) \times 10^{14}\,{\rm M}_{\odot}$. We expect to improve this result substantially by including more spectroscopic data. At the current level, the kinematic mass estimate represents only an upper limit of the mass. The analysis can be improved following, e.g., the method described in detail in Biviano et al. (2006).

8.4.3 X-ray analysis

The cluster was recently serendipitously observed with ACIS on-board *Chandra* with a total integration time of ∼38 ks. In spite of the surface brightness dimming due to the high cluster redshift, we can see extended X-ray emission out to ∼0.5 Mpc. This emission

shows a regular morphology and is clearly elongated in the same direction as the distribution of red galaxies and the projected matter distribution. Our spectral analysis of the *Chandra* data yields a global temperature of $T_{\rm X} = 5.29 \pm 1.02$ keV, and a total mass of $M^{\rm X}_{200} = (3.87 \pm 1.26) \times 10^{14}\,{\rm M}_{\odot}$, in good agreement with Paper I. We applied several tests (different background regions, different X-ray statistics) to check the robustness of our findings, which we conclude are robust against several systematics involved in the X-ray spectral analysis.

Any X-ray study relies on the accuracy achieved for the temperature and electron density distribution of the ICM and thus measure the mass distributions with statistical uncertainties below 15 per cent (e.g. Vikhlinin et al. 2006). However, the accuracy of X-ray cluster mass estimates based on hydrostatic equilibrium is limited by additional physical processes in the ICM (e.g. merger) and projection effect (e.g. substructure). Recently, Zhang et al. (2009) showed that for substructure (see Böhringer et al. 2010) this reflects into $\sim$10 per cent fluctuations in the temperature and electron number density maps. Given the evidence for a cluster bullet and up to six galaxy overdensities in the cluster (see Paper I), these possibly will introduce an additional $\sim$20 per cent systematic error in the mass estimate. Nevertheless, our X-ray analysis is still dominated by the poor statistic of the data in hand.

Note that the X-ray global temperature does not follow the $T_{\rm X}$–σ relation shown in Fig. 32, which would lead to a global temperature of $T_{\rm X} = 2.59$ keV. However, together with the other high-z cluster it is still consistent with the relation within its larger scatter. A similar result has been reported for XMMU J1229+0151 (Santos et al. 2009).

We observe evidence for a $\approx$14 per cent bias in the ratio, $\sigma_{\rm WL}/\sigma_{\rm Kin}$, of the velocity dispersion from the weak lensing and the kinematic analysis against temperature $T_{\rm X}$ for the nine distant ($z > 0.8$) galaxy clusters (right-hand panel of Fig. 32). For XMMU J1230.3+1339 we can infer a ratio $\sigma_{\rm WL}/\sigma_{\rm Kin} = 1.93 \pm 0.42$, which is on the upper end of all clusters. We want to stress here again the lack of statistics for the kinematic analysis, which leads to a large uncertainty in the ratio. Within the large error bars, the ratios of the kinematical and lensing velocity dispersion seem to be the same. The mean average ratio is larger than one (1.14 ± 0.46), but it needs a larger data set to show whether this difference is significant. If the galaxies with measured velocities are still falling into the cluster one would expect a velocity dispersion biased high. The velocity dispersion would be biased low if non cluster member galaxies from the surrounding filaments were considered. Our procedure to eliminate galaxies in the determination of the velocity dispersion is, however, made to avoid the latter effect. The ratio of weak lensing to dynamical velocity dispersion could also be biased high when matter associated with groups correlated to the cluster and along the line of sight is accounted to the cluster in the weak lensing analysis. One caveat in estimating the lensing to dynamical velocity dispersion lies in the reliability of the errors. For instance, some of the clusters have a weak lensing velocity dispersion of around 900 km s^{-1} with a 1σ error of only 50 km s^{-1}, or about 5 per cent. Unless using space data with a high density of objects such an accuracy is very difficult to achieve. Even more so, if one accounts for the fact that clusters at these high redshifts consist of many subclumps, and that the redshift distribution of background objects shows cosmic variance, the weak lensing measurement will be biased.

Given the poor X-ray photon statistics we were able to derive weak constraints on the metal abundance $Z = (0.29 \pm 0.24)\,{\rm Z}_{\odot}$ of the ICM from the detection of the Fe-K line in the *Chandra* spectrum.

8.4.4 Comparison

We estimate independently and self-consistently values of the cluster mass within R_{200}, the radius of the sphere within which the cluster overdensity is 200 times the critical density of the Universe at the cluster redshift, from kinematic, X-ray and weak lensing analyses. The X-ray mass profile, based on the assumptions of isothermal gas in hydrostatic equilibrium, is found to be in good agreement with the mass density profile derived from the kinematic analysis. Given the fact that the weak lensing analysis is performed at the feasibility limit of ground-based observations and therefore leads to larger errors, the weak lensing mass density profile is consistent with the other data within the errors. Note that all our individual mass estimates (see Table 5) are in good agreement with each other. The combined weighted mass estimate $M_{200} = (4.56 \pm 2.3) \times 10^{14}\,{\rm M}_{\odot}$ for XMMU J1230.3+1339 is in very good agreement with the combined mass estimate of Paper I, where a total mass $M_{200} = (4.19 \pm 0.7) \times 10^{14}\,{\rm M}_{\odot}$ is estimated.

9 SUMMARY & CONCLUSIONS

This paper describes the results of the first LBT multicolour and weak lensing analyses of an X-ray selected galaxy cluster from the XDCP, the high redshift cluster XMMU J1230.3+1339 at $z \sim 1$. The high-quality LBT imaging data combined with the FORS2 spectroscopic data allow us to derive accurate galaxy photometry and photometric redshifts.

Our main conclusions are as follows.

(i) The photometric redshift analysis results in an accuracy of $\triangle z/(1+z) = 0.07$ (0.04) and an outlier rate $\eta = 13$ (0) per cent, when using all (secure; ≥ 95 per cent confidence) spectra, respectively.

(ii) We find an $i - z$ against z CMR with a slope of -0.027 and a zero-point of 0.93. Our $i - z$ against z CMR shows also evidence for a truncated RS at $z = 24$, while rich low-redshift systems exhibit a clear sequence down to fainter magnitudes. Similar evidence has been observed for other clusters (e.g. EDisCS clusters; see De Lucia et al. 2007; RXJ1716.4+6708 at $z = 0.81$, see Koyama et al. 2007).

(iii) The cluster clearly follows the Butcher & Oemler effect, with a blue galaxy fraction of $f_b \approx 50$ per cent.

(iv) We see an indication of recent SF in the distribution of the ETG in the $U - B$ against $r - z$ colour–colour diagram.

(v) The BCG could be identified spectroscopically and from photometry as an ETG. A displacement of this galaxy from the X-ray cluster centre of $\sim$100 kpc is observed.

(vi) Compared to XMMU J1229+0151 at $z = 0.97$ (Santos et al. 2009) we observe a similar $i - z$ against z CMR.

(vii) Compared to RDCS J0910+5422 at $z = 1.10$ (Tanaka et al. 2008) we observe also several additional clumps, with similar colours in the CMR.

(viii) We detect a weak lensing signal at 3.5σ significance using the aperture mass technique. Furthermore, we find a significant tangential alignment of galaxies out to a distance of $\sim$4 arcmin or $\sim 1.5\,r_{200}$ from the cluster centre. The S/N peak of the weak lensing analysis coincides with the *Chandra* X-ray centroid.

(ix) We have demonstrated the feasibility of ground-based weak lensing studies of massive galaxy clusters out to $z \sim 1$.

(x) From our X-ray analysis, we obtain a global temperature of $T_{\rm X} = 5.29$ keV and a luminosity of $L_{\rm X}[0.5\text{–}2.0\,{\rm keV}] = 1.48 \times 10^{44}$ erg s^{-1}, within an aperture of 40 arcsec, in good agreement with the results presented in Paper I.

(xi) Mass estimates inferred from the kinematic, weak lensing and X-ray analyses are consistent within their uncertainties. We derive a total mass of $M_{200} = (3.9 \pm 1.3) \times 10^{14}\,\mathrm{M}_{\odot}$, $r_{200} = 1046 \pm 113$ kpc for the X-ray data, which has the smallest uncertainty of the three mass estimates. From the weak lensing NFW likelihood analysis we find a concentration parameter $c = 4.0^{+14}_{-2}$ and a scale radius of $r_{\mathrm{s}} = 344^{+50}_{-57}$ kpc, which is consistent with expectation from simulations (Bullock et al. 2001; Dolag et al. 2004).

(xii) We see evidence for a ≈14 per cent bias in the ratio, $\sigma_{\mathrm{WL}}/\sigma_{\mathrm{Kin}}$, of the velocity dispersion form the weak lensing and the kinematic analysis against temperature T_{X} for distant ($z > 0.8$) galaxy clusters.

We have been awarded 75 ks ACIS-S onboard *Chandra* and an extensive spectroscopic follow-up on ∼100 photo-z selected cluster-members, using FORS2 to complement our data set. Both will be observed in 2010/11. With this additional data we will improve the characterization of this remarkably rich, X-ray luminous galaxy cluster.

ACKNOWLEDGMENTS

This research has made use of the NASA/IPAC Extragalactic Data base (NED) which is operated by the Jet Propulsion Laboratory, California Institute of Technology, under contract with the National Aeronautics and Space Administration.

We are grateful to our anonymous reviewer for helpful comments and recommendations. ML would like to thank A. Bauer, D. Clowe, T. Erben, C. Heymans, H. Hoekstra, Y. Mellier, P. Schneider, T. Schrabback, P. Simon, R. Suhada, P. Spinelli, A. Taylor and L. van Waerbeke for fruitful discussions and helpful comments. This work was supported by the DFG Sonderforschungsbereich 375 'Astro-Teilchenphysik', the DFG priority program 1177, Cluster of Excellence 'Origin of the Universe' and the TRR33 'The Dark Universe'. ML thanks the European Community for the Marie Curie research training network 'DUEL' doctoral fellowship MRTN-CT-2006-036133. HQ thanks partial support from the FONDAP Centre for Astrophysics.

REFERENCES

Abell G., Corwin H., Olowin R., 1989, ApJS, 70, 1
Adelman-McCarthy J. K. et al., 2007, ApJS, 172, 634
Andreon S., Puddu E., de Propris R., Cuillandre J.-C., 2006, MNRAS, 369, 969
Andreon S., 2008, MNRAS, 385, 979
Appenzeller I. et al., 1998, The Mesanger, 94, 1
Arnaud K. A., 1996, in Jacoby G. H., Barnes J., eds, ASP Conf. Ser. Vol. 101. Astronomical Data Analysis Software and Systems V. Astron. Soc. Pac., San Francisco, p. 17
Bacon D. J., Massey R. J., Refregier A. R., Ellis R., 2003, MNRAS, 344, 673
Bartelmann M., Schneider P., 2001, Phys. Rev., 340, 291
Becker R. H., White R. L., Helfand D. J., 1995, ApJ, 450, 559
Beers T. C., Flynn K., Gebhardt K., 1990, AJ, 100, 32
Bender R. et al., 2001, in Cristiani S., Renzini A., Williams R. E., eds, Deep Fields, Proc. ESO Workshop. Springer-Verlag, Heidelberg, p. 96
Benítez N., 2000, ApJ, 536, 571
Benjamin J., van Waerbeke L., Ménard B., Kilbinger M., 2010, MNRAS, 408, 1168
Bertin E., 2008, Swarp v2.17.0 User's Guide
Bertin E., Arnouts S., 1996, A&AS, 117, 393
Bertin E., Marmo C., 2007, Weightwatcher v1.8.6 User's Guide
Biviano A., Murante G., Borgani S., Diaferio A., Dolag K., Girardi M., 2006, A&A, 456, 23
Böhringer H., Werner N., 2010, A&AR, 18, 127
Böhringer H. et al., 2010, A&A, 514, 32
Brimioulle F., Lerchster M., Seitz S., Bender R., Snigula J., 2008, preprint (arXiv: 0811.3211)
Bullock J. S. et al., 2001, MNRAS, 321, 559
Butcher H., Oemler A., Jr,, 1978, ApJ, 219, 18
Butcher H., Oemler A., Jr, 1984, ApJ, 285, 426
Carlberg R. G. et al., 1996, ApJ, 462, 32
Carlberg R. G. et al., 1997, ApJ, 476, L7
Carlberg R. G., Yee H. K. C., Ellingson E., 1997, ApJ, 478, 462
Cavaliere A., Fusco-Femiano R., 1976, A&A, 49, 137
Clowe D., Luppino G. A., Kaiser N., Henry J. P., Gioia I. M., 1998, ApJ, 497, L61
Clowe D., Luppino G. A., Kaiser N., Gioia I. M., 2000, ApJ, 539, 540
De Lucia G. et al., 2007, MNRAS, 374, 809
Demarco R. et al., 2005, A&A, 432, 381
Demarco R. et al., 2007, ApJ, 663, 164
Dickey J. M., Lockman F. J., 1990, ARA&A, 28, 215
Dolag K. et al., 2004, A&A, 416, 853
Donahue M. et al., 1999, ApJ, 527, 525
Drory N., Bender R., Feulner G., Hopp U., Maraston C., Snigula J., Hill G. J., 2004, ApJ, 608, 742
Ebeling H., Jones L. R., Fairley B. W., Perlman E., Scharf C., Horner D., 2001, ApJ, 548, 23
Edge A., Stewart G., 1991, MNRAS, 252, 428
Erben T., Van Waerbeke L., Bertin E., Mellier Y., Schneider P., 2001, A&A, 366, 717
Erben T. et al., 2009, A&A, 493, 1197
Ettori S., 2000, MNRAS, 311, 313
Fassbender R., 2008, preprint (arXiv:0806.0861)
Fassbender R. et al., 2010, A&A, preprint (arXiv:1009.0264) (Paper I)
Fioc M., Rocca-Volmerange B., 1997, A&A, 326, 950
Gabasch A. et al., 2004a, A&A, 441, 41
Gabasch A. et al., 2004b, ApJ, 616, 83
Gabasch A. et al., 2006, A&A, 448, 101
Gabasch A., Goranova Y., Hopp U., Noll S., Panella M., 2008, MNRAS, 383, 1319
Gal R. R., Lubin L. M., Squires G. K., 2004, ApJ, 607, 1
Giallongo E. et al., 2008, A&A, 482, 349
Gioia I. M., Henry J. P., Mullis C. R., Ebeling H., Wolter A., 1999, AJ, 117, 2608
Gladders M. D., Yee H. K. C., 2000, AJ, 120, 2148
Goto T. et al., 2005, ApJ, 621, 188
Haines C. P. et al., 2009, ApJ, 704, 126
Heymans C. et al., 2006, MNRAS, 368, 1323
Heymans C. et al., 2008, MNRAS, 385, 1431
Hill J. M., Salinari P., 1998, Proc. SPIE, 3352, 23
Hilton M. et al., 2010, ApJ, 718, 133
Hoekstra H., 2003, MNRAS, 339, 1155
Hoekstra H., 2007, MNRAS, 379, 317
Hoekstra H., Jain B., 2008, Ann. Rev. Nuc. Part. Sci. 58, 99
Hoekstra H., Franx M., Kuijken K., Squires G., 1998, ApJ, 504, 636 (KSB+)
Hoekstra H., Franx M., Kuijken K., 2000, ApJ, 532, 88
Ilbert O. et al., 2006, A&A, 457, 841
Jee M. J., Tyson J. A., 2009, ApJ, 691, 1337
Jee M. J. et al., 2005a, ApJ, 618, 46
Jee M. J. et al., 2005b, ApJ, 634, 813
Jee M. J. et al., 2006, ApJ, 642, 720
Jee M. J. et al., 2009, ApJ, 704, 672
Kaastra J. S., 1992, Internal SRON-Leiden Report, updated version 2.0, 1992
Kaiser N., Squires G., 1993, ApJ, 404, 441
Kaiser N., Squires G., Broadhurst T., 1995, ApJ, 449, 460 (KSB)
Kausch W., Gitti M., Erben T., Schindler S., 2007, A&A, 471, 31
Kaviraj S., Kirkby L. A., Silk J., Sarzi M., 2007, MNRAS, 382, 960
Kocevski D. D. et al., 2009, ApJ, 690, 295

Koyama Y., Kodama T., Tanaka M., Shimasaku K., Okamura S., 2007, MNRAS, 382, 1719
Liedahl D. A., Osterheld A. L., Goldstein W. H., 1995, ApJ, 438, L115
Lombardi M. et al., 2005, ApJ, 623, 42
Luppino G. A., Gioia I. M., 1995, ApJ, 445, L77
Luppino G., Kaiser N., 1997, ApJ, 475, 20
Margoniner V. E., Lubin L. M., Wittman D. M., Squires G. K., 2005, AJ, 129, 20
Massey R. et al., 2007, MNRAS, 376, 13
Maughan B. J., Ellis S. C., Jones L. R., Mason K. O., Córdova F. A., Priedhorsky W., 2006, ApJ, 640, 216
Maughan B. J., Jones C., Jones L. R., Van Speybroek L., 2007, ApJ, 659, 1125
Maughan B. J., Jones C., Jones L. R., Forman W., Van Speybroek L., 2008a, ApJS, 174, 117
Maughan B. J. et al., 2008b, MNRAS, 387, 998
McCracken H. J. et al., 2003, A&A, 410, 17
Medezinski E. et al., 2010, MNRAS, 405, 257
Mei S. et al., 2009, ApJ, 690, 42
Mellier Y., 1999, ARA&A, 37, 127
Menci N. et al., 2008, ApJ, 685, 863
Mewe R., Gronenschild E. H. B. M., van den Oord G. H. J., 1985, A&AS, 62, 197
Mewe R., Lemen J. R., van den Oord G. H. J., 1986, A&AS, 65, 511
Monet D. G., 1998, A&AS, 19312003
Mullis C. R. et al., 2005, ApJ, 623, 85
Navarro J., Frenk C., White S., 1996, ApJ, 462, 563
Navarro J., Frenk C., White S., 1997, ApJ, 486, 493
Pacaud F. et al., 2007, MNRAS, 383, 1289
Papovich C. et al., 2010, ApJ, 716, 1503
Pello R. et al., 2009, A&A, 508, 1173
Pickles A. J., 1998, PASP, 110, 863
Pimbblet K. A., Smail I., Edge A., O'Hely E., Couch W. J., Zabludoff A. I., 2006, MNRAS, 366, 651
Radovich M., Puddu E., Romano A., Grado A., Getman F., 2008, A&A, 487, 55
Romano A. et al., 2010, A&A, 514, 88
Rosati P., Borgani S., Norman C., 2002, ARA&A, 40, 539
Rosati P., Tozzi P., Gobat R., 2004, AJ, 127, 230
Rosati P., Tozzi P., Gobat R., 2009, A&A, 508, 583
Rovilos E. et al., 2009, A&A, 507, 195
Santos J. S. et al., 2009, A&A, 501, 49
Schade D., 1997, in Tanvir N. R., Aragon-Salamanca A., Wall J. V., eds, The Hubble Space Telescope and the High Redshift Universe. World Scientific, Singapore
Schlegel D. J., Finkbeiner D. P., Davis M., 1998, ApJ, 500, 525
Schneider P., 1996, MNRAS, 283, 837
Schneider P., Bartelmann M., 1997, MNRAS, 286, 696
Schneider P., Van Waerbeke L., Jain B., Kruse G., 1998, MNRAS, 296, 873
Schneider P., King L., Erben T., 2000, A&A, 353, 41
Schrabback T. et al., 2007, A&A, 468, 823
Speziali R. et al., 2008, Proc. SPIE, 7014, 158
Stanford S. A. et al., 2006, ApJ, 646, 13
Tanaka M. et al., 2005, MNRAS, 362, 268
Tanaka M. et al., 2008, A&A, 489, 571
Tanaka M., Finoguenov A., Ueda Y., 2010, ApJ, 716, 152
Taylor A. N. et al., 2004, MNRAS, 353, 1176
Tran K. et al., 2007, ApJ, 661, 750
Ulmer M. P. et al., 2009, A&A, 503, 399
Van Waerbeke L. et al., 2001, A&A, 374, 757

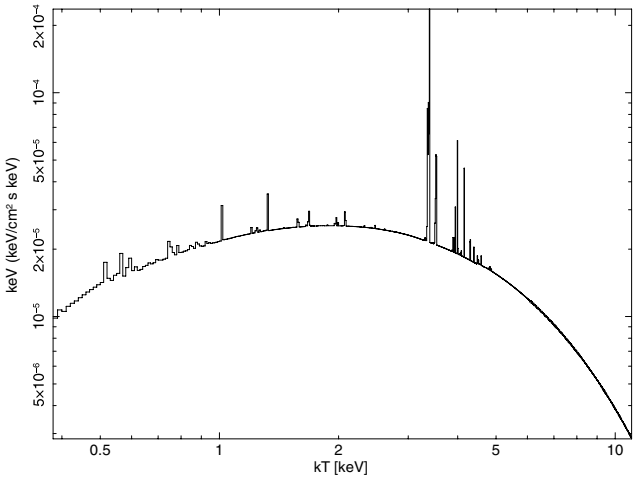

Figure A1. Absorbed ICM model spectrum of the bremsstrahlung continuum and line emission for a plasma at a redshift of $z = 0.975$ with $Z/Z_{\odot} = 0.3$ and temperature of $T = 5.29$ keV observed through a galactic hydrogen column density of $N_{\rm H} = 2.64 \times 10^{22}\,{\rm cm}^{-2}$. The redshifted Fe K-line (6.7 keV at rest frame) is visible at 3.3 keV.

Vikhlinin A. et al., 2006, ApJ, 640, 691
Visvanathan N., Sandage A., 1977, ApJ, 216, 214
White S. D. M. et al., 2005, A&A, 444, 365
Yahil A., Vidal N. V., 1977, ApJ, 214, 347
Yi S. K., 2008, in Herber U., Jeffery C. S., Napiwotzki R., eds, ASP Conf. Ser. Vol. 392, Hot Subdwarf Stars and Related Objects. Astron. Soc. Pac., San Francisco, p. 3
Zabludoff A. I., Huchra J. P., Geller M. J., 1990, ApJS, 74, 1
Zhang Y.-Y., Reiprich T. H., Finoguenov A., Hudson D., Sarazin C. L., 2009, ApJ, 699, 1178

APPENDIX A: ICM MODEL SPECTRA

An absorbed ICM model spectrum of the bremsstrahlung continuum and line emission for a plasma, representing the galaxy cluster, is shown in Fig. A1.

APPENDIX B: PSF ANISOTROPY PATTERN

In Fig. B1, we plot the measured PSF patterns of all six bands, represented by the unsaturated stars imaged on the field at high S/N. The measured PSF widths of stars on the stacks are summarized in Table 1.

APPENDIX C: HIGH-z CLUSTER

In Table C1, we give an overview of recently studied high-z galaxy clusters. So far, only 10 of them were studied with weak lensing. Note that only XMMU J1230.3+1339 ($z \sim$1), ClG J1604+4304 ($z \sim$0.9), RX J1716.6+6708 and ClG 1137.5+6625 ($z \sim$0.8) have a weak lensing detection based on ground-based data.

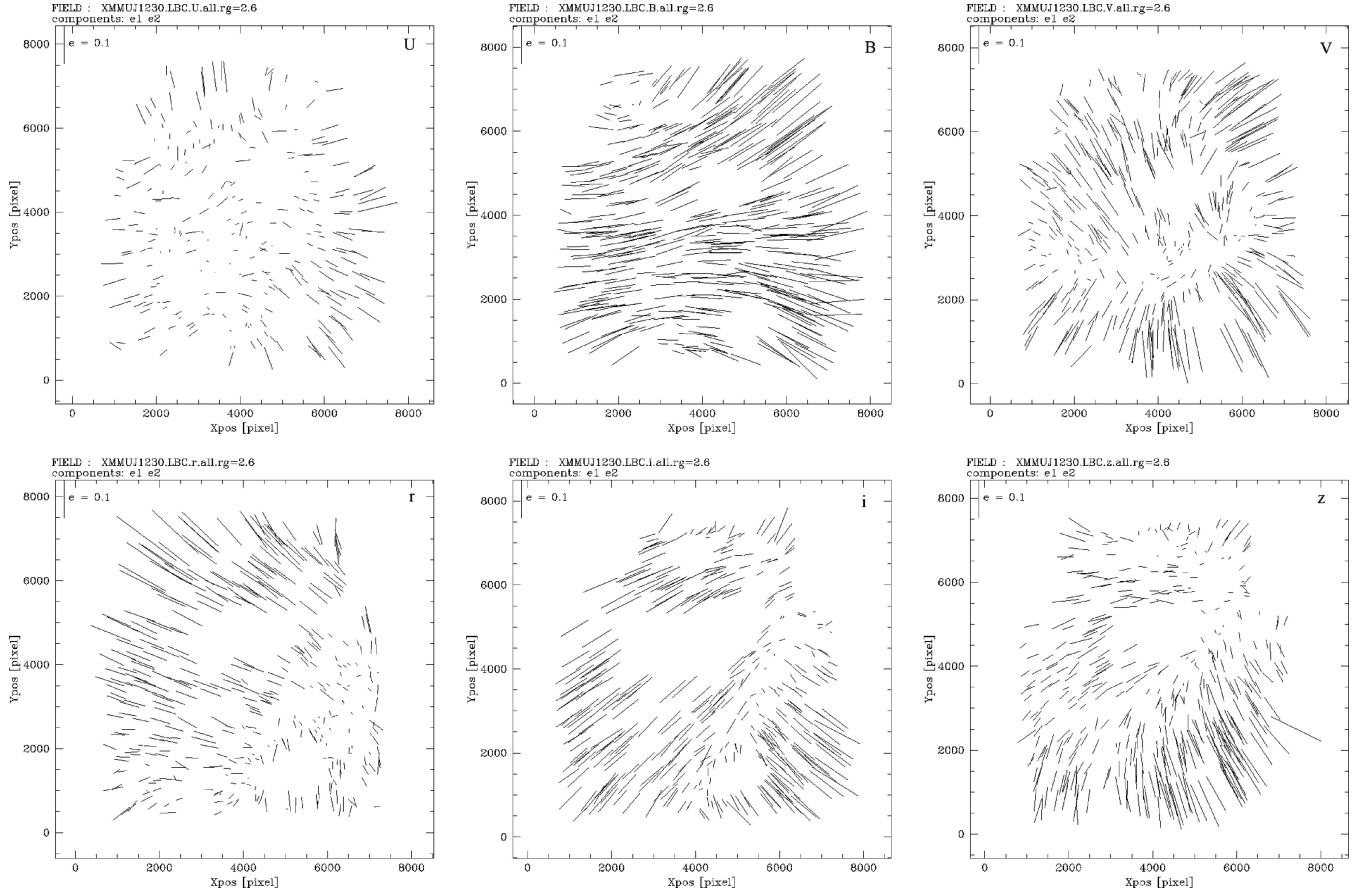

Figure B1. PSF anisotropy pattern of the image stacks in the six (U, B, V, r, i, z) filters. The sticks mark the observed ellipticities of high S/N but unsaturated stars in the image stacks. The direction of the sticks coincides with the major axis of the PSF, the length is indicating the degree of anisotropy. An ellipticity of 10 per cent is shown in the upper-left corner of each panel. The definition of ellipticity is given in equation (4). The measured PSF widths of stars on the stacks are summarized in Table 1.

Table C1. List of high-z galaxy clusters and their basic optical/X-ray/weak lensing properties: (1) sequence number, (2) right ascension, (3) declination, (4) number of spectroscopic objects used to estimate the cluster redshift (6) and the line-of-sight velocity dispersion (7), (8) bolometric X-ray luminosity, (9) ICM temperature, (10) velocity dispersion from a weak lensing analysis, more information on peculiar individual clusters is provided in the associated reference (11).

ID	Cluster name	RA (J2000)	Dec. (J2000)	$N_{\rm gal}$	Redshift	$\sigma_l^{\rm Kin}$ (km s^{-1})	$L^x_{\rm bol}$ (10^{44} erg s^{-1})	$T_{\rm X}$ (keV)	$\sigma^{\rm WL}_{\rm SIS}$ (km s^{-1})	Ref.
(1)	(2)	(3)	(4)	(5)	(6)	(7)	(8)	(9)	(10)	(11)
1	SXDF-XCLJ0218-0510	$02^{\rm h}18^{\rm m}21\overset{\rm s}{.}3$	$-05^\circ10'27''$	9	1.6230 ± 0.001	537 ± 213	0.34 ± 0.16	1.7 ± 0.3	... ±...	Tanaka, Finoguenov & Ueda (2010); Papovich et al. (2010)
2	XMMXCS J2215.9-1738	$22^{\rm h}15^{\rm m}58\overset{\rm s}{.}5$	$-17^\circ38'03''$	31	1.457 ± 0.001	720 ± 110	2.92 ± 0.35	4.1 ± 0.9	... ±...	Hilton et al. (2010); Stanford et al. (2006)
3	XMMU J2235.3-2557	$22^{\rm h}35^{\rm m}20\overset{\rm s}{.}8$	$-25^\circ57'40''$	30	$1.390 \pm ...$	802 ± 77	8.5 ± 0.4	8.6 ± 1.3	1145 ± 70	Jee et al. (2009a); Rosati, Tozzi & Gobat (2009); Mullis et al. (2005)
4a	ClG J0848+4453, Lynx W	$08^{\rm h}48^{\rm m}34\overset{\rm s}{.}7$	$+44^\circ53'42''$	9	$1.273 \pm ...$	650 ± 170	1.5 ± 0.8	1.7 ± 0.7	762 ± 133	Mei et al. (2009);
4b	ClG J0849+4452, Lynx E	$08^{\rm h}48^{\rm m}56\overset{\rm s}{.}3$	$+44^\circ52'16''$	11	$1.261 \pm ...$	720 ± 140	2.1 ± 0.5	3.8 ± 1.3	740 ± 134	Jee et al. (2006)
5	RDCS J1252.9−2927	$12^{\rm h}52^{\rm m}48\overset{\rm s}{.}0$	$-29^\circ27'00''$	38	1.2370 ± 0.0004	747 ± 84	6.6 ± 1.1	6.0 ± 0.7	1185 ± 120^{21}	Demarco et al. (2007); Lombardi et al. (2005); Rosati, Tozzi & Gobat (2004)
6	RDCS J0910+5422	$09^{\rm h}10^{\rm m}00\overset{\rm s}{.}0$	$-54^\circ22'00''$	161	1.1005 ± 0.0016	716 ± 141	2.9 ± 0.4	2.9 ± 0.4	... ±...	Maughan et al. (2008a); Tanaka et al. (2008)
7	XLSSJ022404.1–041330	$02^{\rm h}24^{\rm m}04\overset{\rm s}{.}1$	$-04^\circ13'30''$	5	$1.050 \pm ...$	... ±...	4.5 ± 0.1	4.3 ± 1.1	... ±...	Maughan et al. (2008b); Pacaud et al. (2007)
8	RzCS052	$02^{\rm h}21^{\rm m}42\overset{\rm s}{.}0$	$-03^\circ21'47''$	21	$1.016 \pm ...$	710 ± 150	... ±...	... ±...	... ±...	Andreon et al. (2008)
9	XMMU J1229.4+0151	$12^{\rm h}29^{\rm m}29\overset{\rm s}{.}2$	$+01^\circ51'26''$	27	0.975 ± 0.001	683 ± 62	$3.0 \pm ...$	6.4 ± 0.7	... ±...	Santos et al. (2009)
10	XMMU J1230.3+1339	$12^{\rm h}30^{\rm m}16\overset{\rm s}{.}0$	$+13^\circ39'04''$	13	0.9745 ± 0.002	657 ± 277	6.5 ± 0.68	5.29 ± 1.02	1308 ± 284	This work & Paper I
11a	ClG J1604+4304	$16^{\rm h}04^{\rm m}23\overset{\rm s}{.}7$	$+43^\circ04'52''$	67	$0.9001 \pm ...$	962 ± 141	$1.576 \pm ...$	3.5 ± 1.82	1004 ± 199	Kocevski et al. (2009); Margoniner et al. (2005);
11b	ClG J1604+4314	$16^{\rm h}04^{\rm m}25\overset{\rm s}{.}8$	$+43^\circ14'23''$	62	$0.8652 \pm ...$	719 ± 71	$1.164 \pm ...$	1.6 ± 0.65	... ±...	Gal, Lubin & Squires (2004)
12	ClG J1226+3332	$12^{\rm h}26^{\rm m}58\overset{\rm s}{.}1$	$+33^\circ32'47''$	6	0.8877 ± 0.004	1650 ± 930	5.12 ± 0.12	10.4 ± 0.6	880 ± 50	Jee et al. (2009b); Maughan et al. (2007); Ebeling et al. (2001)
13	RX J1257.2+4738	$12^{\rm h}57^{\rm m}12\overset{\rm s}{.}2$	$+47^\circ38'07''$	18	$0.866 \pm ...$	$600 \pm ...$	... ±...	3.6 ± 2.9	... ±...	Ulmer et al. (2009)
14	ClG 1054–0321	$10^{\rm h}57^{\rm m}00\overset{\rm s}{.}2$	$-03^\circ37'27''$	129	$0.826 \pm ...$	1156 ± 82	3.1 ± 0.1	8.9 ± 1.0	1150 ± 51	Tran et al. (2007); Jee et al. (2005b); Hoekstra et al. (2000)
15	ClG J0152–1357	$01^{\rm h}52^{\rm m}41\overset{\rm s}{.}0$	$-13^\circ57'45''$	102	0.837 ± 0.001	1632 ± 115	... ±...	6.46 ± 1.74	903 ± 57	Jee et al. (2005a); Demarco et al. (2005); Maughan et al. (2006)
16	RX J1716.6+6708	$17^{\rm h}16^{\rm m}49\overset{\rm s}{.}6$	$+67^\circ08'30''$	37	0.809 ± 0.0051	1522 ± 215	1.50 ± 0.4	5.7 ± 1.4	$1030 \pm ...$	Clowe et al. (2000); Gioia et al. (1999)
17	ClG 1137.5+6625	$11^{\rm h}40^{\rm m}23\overset{\rm s}{.}3$	$-66^\circ09'01''$	22	0.784 ± 0.0003	884 ± 185	1.90 ± 0.4	5.7 ± 2.1	$1190 \pm ...$	Clowe et al. (1998); Luppino et al. (1995); Donahue et al. (1999)

This paper has been typeset from a TEX/LATEX file prepared by the author.